Solidification and grown-in defects

Thierry Duffar

Solidification and Grown-in Defects

Thierry Duffar

This chapter is dedicated to my colleague Marie-Danielle Dupouy, who died in September 2004. She devoted her scientific activity to the study of the effect of liquid convection on metallurgical alloy structures. We were working together, with the help of numerous colleagues and students, on an academic project that ultimately fed the present text.

3.1
Introduction: the Solid–Liquid Interface

Most solid alloys are prepared from the liquid phase, and the liquid-to-solid transformation, called solidification, is the topic of this chapter.

Obviously, the structure, defects, and properties found in the final alloy are the result of what happened in the elaboration process and therefore first in the liquid phase, where transport phenomena, diffusion and convection, have a strong influence on the final structure. The main and special solidification features occur at the transition between the solid and the liquid phases, the so-called solid–liquid interface. The physics of what happens later in the solid phase is covered by other chapters in this book: this one will deal essentially with the solid–liquid interface and its interaction with the liquid.

This introduction will be completed with some fundamental notions relating to this interface. Section 3.2 will present the classical theories of structures in alloy solidification: stability of the solid–liquid interface, growth of dendrites and eutectics and rapid solidification; it will be seen that the diffusion in the liquid state plays a major role in these processes. Section 3.3 will be focused on the defects resulting from solidification processes, and the role of convection in the liquid will be stressed.

3.1.1
Structure of the Solid–Liquid Interface

There are essentially two different structures of a solid–liquid interface. The ''faceted'' interface is represented by a flat, smooth surface, at the atomic scale.

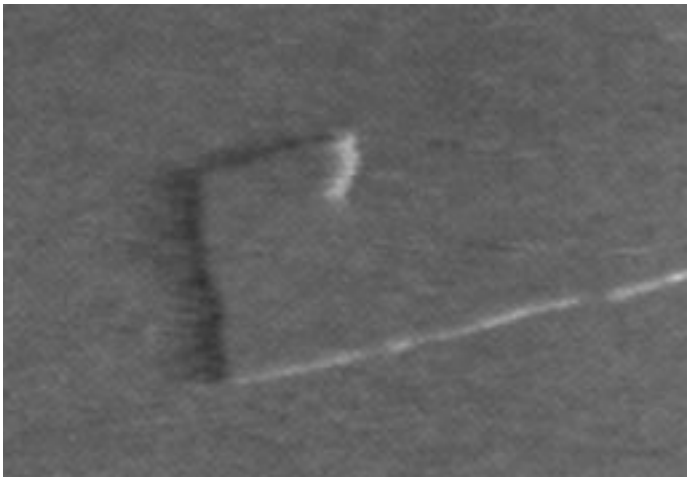

Fig. 3.1 AFM observation of a (101) facet on a growing monoclinic lysozyme crystal. An unsaturable spiral step, likely to be associated with a dislocation, is visible (Chernov et al. 2004).

Therefore there is a sharp, total change in the degree of order when crossing the interface, from the fully crystalline solid side to the liquid (Fig. 3.1).

In ''rough'' interfaces, the transition between the fully ordered solid and the disordered liquid is less abrupt, extending over several atomic distances (Fig. 3.2). In this layer, atoms, molecules, or building units are experiencing an environment of which the degree of order is fluctuating with time. Results of molecular dynamics simulations have shown that the unit movements do not change markedly when crossing the interface (at the melting temperature). Structural and kinetic models of such diffuse interfaces have been proposed; see for example the pioneering work of J. W. Cahn (1960), and more sophisticated models of

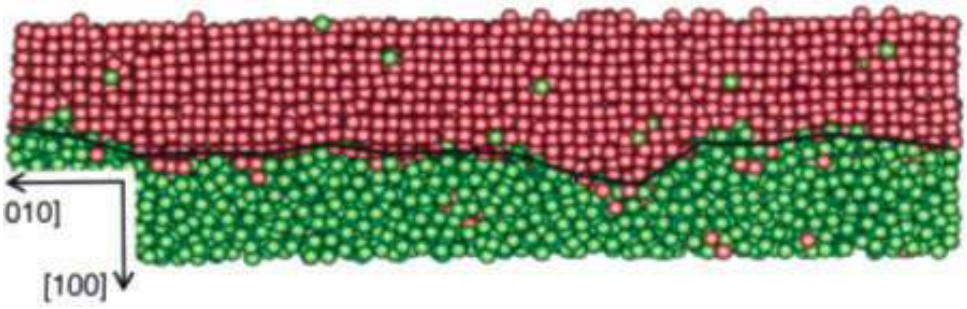

Fig. 3.2 Liquid–solid transition through a diffuse zone with a thickness of a few structural units (Hoyt et al. 2004).

Table 3.1 Observed morphology of the crystal surface during growth of various materials in several processes.

Reduced entropy α	Material	Feeding phase	Morphology
~1	metal	molten liquid	rough
~1	crystalline polymer	molten liquid	rough
2–3	semiconductor	solution	rough to faceted
~10	metal	vapor	faceted

the interface can be found in the review article by Bennema (1993), but for the purpose of the present discussion simplified surface representations will be used.

Theoretical models have been proposed in order to predict the interface roughness. The most classical, from K. Jackson (1958) takes into account the transformation entropy (vaporization, solution, melting) reduced to the ideal gas constant R [Eq. (1)].

$$\alpha = \frac{\Delta S_t}{R} \tag{1}$$

Faceting occurs if $\alpha > 2$.

3.1.2 Kinetics of the Solid–Liquid Interface

Solidification generally occurs under thermal or chemical gradients and cannot be considered as an equilibrium process. However, a local thermodynamic equilibrium on the interface can be considered in the case where, on arrival, a building unit can easily find a satisfactory position in its surroundings. By denoting the surface diffusion coefficient as D_S and the typical size of a structural unit as a, the surface velocity V_u of the unit can be compared with the interface velocity v_i by Eq. (2)

$$\frac{V_u}{v_i} = \frac{D_S}{a v_i} \tag{2}$$

With typical values of D_S and a (5×10^{-10} m^2 s^{-1} and 5×10^{-10} m) it can be seen that for interface velocities higher than 1 m s^{-1} the local thermodynamical equilibrium does not apply. This case will be treated in Section 3.2.3 (Rapid Solidification).

For lower velocities, thermodynamic data, especially the phase diagram in the case of alloys, can be used safely. For example, the temperature T_i of an alloy

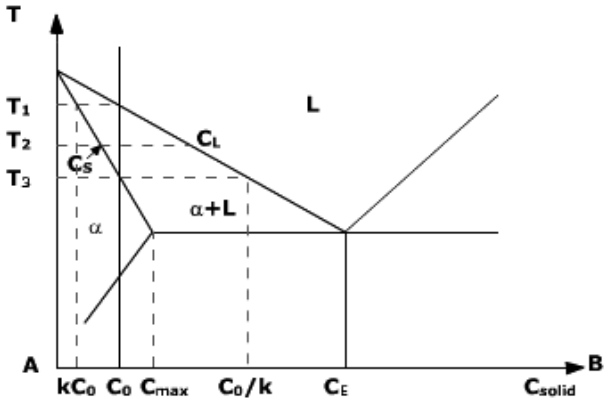

Fig. 3.3 Typical phase diagram used in this chapter.

interface can be computed from the liquidus slope (which is generally negative; see Fig. 3.3), by Eq. (3).

$$T_i = T_m + \mathrm{m_l} c_i \tag{3}$$

However, thermodynamic equilibrium is established only in the case of a resting interface. In order to make it move, it is necessary to introduce a slight deviation from equilibrium. In the case of solidification this is kinetic undercooling, measured as the difference between the thermodynamic melting temperature T_m and the actual temperature T_i of the moving interface [Eq. (4)].

$$\Delta T_k = T_m - T_i \tag{4}$$

In the case of the faceted interface, growth can occur only by nucleation of a cluster on the perfectly flat surface. When this cluster is created, the whole surface is quickly covered, so that the factor limiting the velocity is the cluster creation step. This gives an interface velocity varying exponentially with undercooling, and then growth only occurs at high values of undercooling, when the cluster size is small enough to have some chance of appearing spontaneously thanks to the density fluctuations of the liquid phase.

Undercooling values of several 10 K result; experiments show, however, that the undercooling for faceted interfaces is generally of the order of a few degrees only. In practice, facets contain defects such as steps and kinks or unsaturable defects such as screw dislocations (see Fig. 3.1). Following the pioneering work of Burton, Cabrera, and Frank (Burton et al. 1951), numerous authors have derived relationships, such as Eq. (5), between the velocity and the undercooling for an imperfect faceted interface.

$$v_i = K_f \Delta T_k^{\,n} \quad 1 < n < 4 \tag{5}$$

K_f is the kinetic coefficient, depending on the number of defects on the surface and also on its crystallographic orientation.

In the case of the rough interface, the interface velocity is calculated from the balance of the structural units coming from the liquid to the interface and leaving the interface for the liquid phase. To a first order, with some simplifying assumptions ([111] surface composed of cubic structural units), Eq. (6) can be shown to hold (Kurz and Fisher 1998).

$$v_i = K_r \Delta T_k \tag{6}$$

K_r is of the order of 1, showing that for classical metallurgical or crystal growth rates (10^{-6}–10^{-4} m s^{-1}) the kinetic undercooling is very low for rough interfaces and can be neglected.

3.1.3
Chemistry of the Solid–Liquid Interface: the Segregation Problem

Figure 3.3 shows a typical, simplified phase diagram of a binary alloy. For a given temperature, T_2, the composition of the solid is related to the composition of the liquid by the segregation coefficient k [Eq. (7)].

$$k = \frac{c_s}{c_l} \tag{7}$$

In most cases, the solid is less concentrated than the liquid ($k < 1$) and this situation will be considered throughout this chapter; the reverse situation ($k > 1$) leads to symmetric results. In case of faceted growth, k is likely to depend on the crystallographic orientation of the interface.

It follows that the advancing interface rejects solute in the liquid and a balance of the incorporated and rejected solute gives the flux toward the liquid [Eq. (8)].

$$-D_l \left(\frac{\partial c}{\partial z}\right)_i = v_i c_i^l (1 - k) \tag{8}$$

This flux generates a boundary layer in the liquid, close to the interface. If diffusive conditions prevail in the liquid, the boundary layer thickness is of the order of δ [Eq. (9)].

$$\delta = \frac{D_l}{v_i} \tag{9}$$

In this case, after an initial transient (whose length is of the order of D_i/kv_i) corresponding to the building of the solute boundary layer, Tiller et al. (1953) have shown that a steady state is obtained, with a growing solid of initial composition

c_0 in equilibrium with a liquid of composition c_0/k. This result is valid as far as the diffusive solute boundary layer is not affected by convection. According to Eq. (9), this is more likely for high interface velocities (even with a growth rate of 10^{-3} m s^{-1}, for a typical diffusion coefficient of 10^{-8} m^2 s^{-1}, the boundary layer is 10 μm thick, and likely to be affected by the convection, which vanishes very close to the interface where solid is growing).

The very general case, then, is that the liquid is mixed by some natural or forced convection and the boundary layer thickness depends on the intensity of convection. If the mixing is strong enough, the solute boundary layer can be neglected and the liquid can be considered as homogeneous. Scheil and Gulliver derived Eq. (10) for the relationship between solid composition c_s and solidified fraction (Scheil, 1942).

$$c_s = kc_0(1 - f_s)^{(k-1)} \tag{10}$$

Figure 3.4 gives the shape of this segregation behavior for different values of k. This equation is not valid right up to the end of the ingot, where the concentration tends toward infinity. In practice different phenomena may occur when the concentration increases, such as precipitation of eutectic material, variation of k with c, or destabilization of the interface (see Section 3.2.1).

For a moderate convection, Burton, Prim and Schlichter (Burton et al. 1953) have shown that Eq. (10), and consequently Fig. 3.4, can be used provided that k is replaced by an "effective" segregation coefficient, k_{eff}, depending on the boundary layer thickness. Its value varies between 1 (the diffusive case seen above) and k (fully mixed liquid, Scheil–Gulliver law); for the interested reader there is a general discussion of these matters, with the calculation of k_{eff} in some configurations, in Garandet et al. (1994).

In the above explanations, cases have been considered where the diffusion of the solute in the solid is negligible, which generally is the case (substitutional alloys). However, this is not valid for solutes of small atoms in lattices of large atoms, as for example in the case of C in Fe (interstitial alloys). If solid diffusion is rapid, on the scale of the solidification time, the solid can be considered homogeneous at any time, especially at the end of solidification, and in equilibrium with the liquid interface composition. In the case of ideal mixing of the liquid, this leads to the well known lever rule, Eq. (11).

$$c_s f_s + c_l f_l = c_s f_s + \frac{c_s}{k}(1 - f_s) = c_0 \tag{11}$$

The chemical segregation problem is unavoidable. Strong mixing of the melt increases the local homogeneity of the solid but increases the macrosegregation all along the ingot. The only way to reduce the segregation is to feed the crucible continuously with fresh solvent in order to keep the liquid composition constant, but this leads to process complexity and this solution is seldom used.

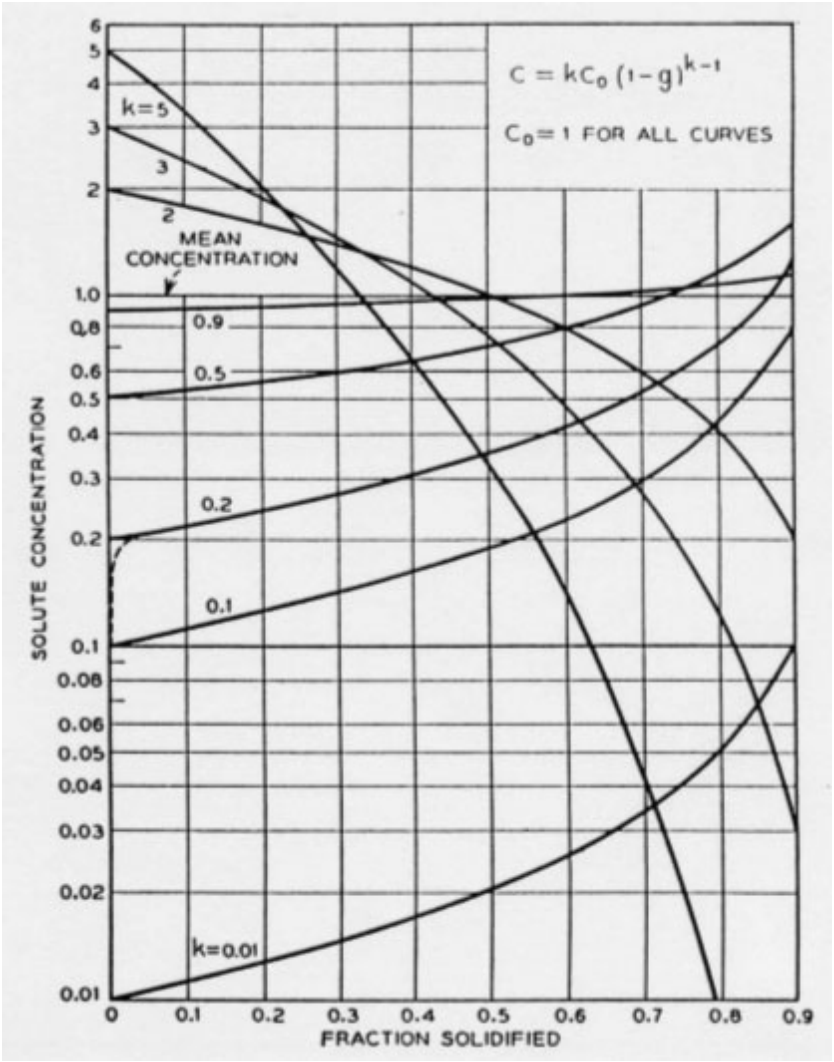

Fig. 3.4 Concentration profile along a solidified ingot for various values of the segregation coefficient k (Garandet et al. 1994).

3.1.4
Temperature of the Solid–Liquid Interface

The nucleation theory (for details, see Chapter 7) can be applied to solidification and, from Gibbs's classical treatment, it appears that the critical nucleation radius in a liquid showing a certain undercooling can be expressed as Eq. (12), where Γ is the Gibbs coefficient (close to 1×10^{-7} K m for metals).

$$r^* = \frac{2\gamma_{ls}}{\Delta S_m \Delta T} = \frac{2\Gamma}{\Delta T} \tag{12}$$

It follows that any curved solid–liquid interface (even at rest) in equilibrium with its liquid shows a capillary undercooling depending on the local curvature κ, according to Eq. (13).

$$\Delta T_{cap} = \Gamma\kappa. \tag{13}$$

This effect is significant only for a radius of curvature of the interface less than 10 μm.

From the above considerations, it follows that the temperature of the solid–liquid interface depends on the chemical composition, on its velocity, and on its curvature. For example, the interface temperature of an alloy growing with a rough interface should be expressed as Eq. (14), from Eqs. (3), (6), and (13), where T_m is the thermodynamic melting point of the pure substance.

$$T_i = T_m + m_l c_i - \frac{v_i}{K_r} - \Gamma\kappa \tag{14}$$

This equation of state of the solid–liquid interface defines its position and shape. The next Section aims to present some classical studies of the solid alloy structures that result from the interaction of Eq. (14) with the thermal and chemical fields surrounding the interface.

3.2
Solidification Structures

The solid–liquid interface morphology changes with the process parameters alloy composition, thermal gradient, and solidification rate. Figure 3.5 shows how it changes when the solidification rate increases. Similar diagrams can be plotted as a function of the alloy composition or thermal gradient.

Derivations of the most important characteristics of the diagram in Fig. 3.5, i.e., the interface destabilization, which corresponds to the transition between planar (a) and cellular (b) interface, the periodicity of the cellular structure (b), the characteristics of the dendrite field (c), and the transition toward rapid solidification (d), are given below. Another case is included, when an eutectic structure is obtained with two different solid phases growing simultaneously from a single liquid.

In practical applications, three regimes are used in order to grow materials.

- Planar interface growth is used to get high-quality single crystals for electronics, optics, detectors, and so on.

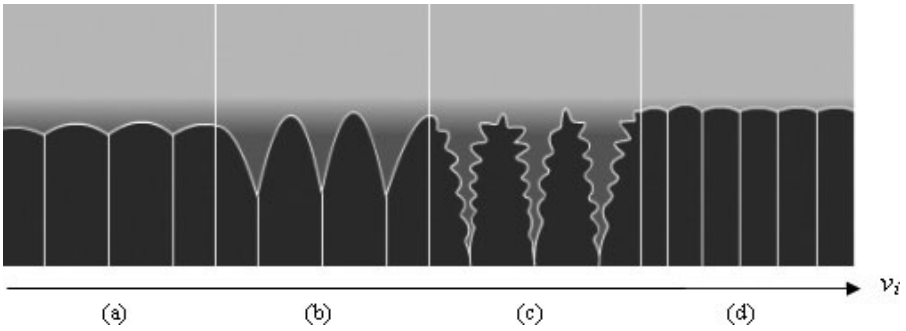

Fig. 3.5 Evolution of the solid–liquid interface morphology with increasing velocity. (a) Planar interface generally observed in single-crystal growth; (b) cellular structures; (c) dendrites observed in classical metallurgical processes; (d) flat interface obtained in rapid solidification.

- Dendritic growth is the most common because it is used universally for all metallurgical processes: steel, cast iron, Al- and Cu-based alloys, and others. The reason is that the dendritic regime leads to tiny microstructures, furthermore accompanied by eutectic areas, and this gives excellent mechanical properties to these alloys.
- Rapid solidification is used in order to obtain very small microstructures and amorphous materials. It is also a way to get metastable phases that cannot be solidified at lower growth rates.

3.2.1 The Interface Stability and Cell Periodicity

Morphological destabilization of the solid–liquid interface is a mechanism aiming to increase its area in order to exchange solute or heat better with the surrounding liquid. This generally leads to important modifications of the structural quality of an alloy and has deserved continuous attention, considering the practical importance of solidification in material processes (Coriell and Mc Fadden 1993).

Destabilization occurs when a perturbation of the interface is likely to expand toward the liquid instead of decreasing and vanishing. To the first order, this can be checked by comparing the actual thermal field in the sample and the local melting temperature, which depends essentially, for a flat interface, on the local chemical composition [Eq. (3)]. Due to the chemical boundary layer at the interface, the chemical composition decreases, and the melting temperature increases, with the distance to the interface. The variation of melting temperature at the interface, toward the liquid, is given by Eq. (15), from Eqs. (3) and (8).

$$\left(\frac{dT_m}{dz}\right)_i = \frac{dT_m}{dc}\left(\frac{dc}{dz}\right)_i = -m_l \frac{v_i c_i^l (1-k)}{D_l} \tag{15}$$

If the thermal gradient in the liquid, at the interface, is lower than this value, a liquid layer close to the interface is at a temperature lower than its melting temperature and any perturbation of the interface will grow toward the liquid. On the contrary, in a high enough liquid thermal gradient, there is no undercooled liquid layer. It follows that the interface stability is written as Eq. (16).

$$\nabla T_i^l > -m_l \frac{v_i c_i^l (1-k)}{D_l} \tag{16}$$

As explained in the Introduction, the composition at the interface, c_i, is likely to change all through the solidification process (see for example Eq. (10) in the case of complete mixing). For a solute rejected into the liquid, the concentration increases continuously and destabilization occurs toward the end of the ingot. It is only in the case of pure diffusion in the liquid that the composition at the interface reaches a steady-state value, c_0/k.

These destabilization mechanisms and criteria were initially proposed by Tiller et al. (1953) and are in acceptable agreement with the experimental observation of destabilization for slow growth rates. However they do not take into account the energy cost linked to the increase in the interface area; taking this into account will make it possible to find the typical size of the resulting structure. This analysis has been performed by Mullins and Sekerka (1964) by studying the effect of a sinusoidal perturbation of the interface, of amplitude ε and period λ, on the thermal and chemical field around it and taking into account the effect of the interface curvature on its temperature [Eq. (13)]. This gives the rate of variation of the perturbation amplitude as in Eq. (17), where Λ and ∇T are mean values taken from the liquid and solid regions, and the ξ are positive functions of the growth rate.

$$\frac{1}{\varepsilon}\frac{d\varepsilon}{dt} = m_l \nabla c \xi_c - \Lambda \nabla T \xi_T - \Gamma \frac{4\pi^2}{\lambda^2} \tag{17}$$

Looking at the right-hand side of Eq. (17), it appears that the first term, related to the solute field, is positive and therefore is the source of the destabilization, whereas the other two terms, related to the thermal field and to the capillarity, are negative and thus stabilize the interface.

From the physical point of view, the interface deformation is an increase in its area in order to improve the rejection of solute toward the liquid. However it is then more difficult to extract the latent heat toward the solid: this explains the stabilizing effect of the thermal field. Furthermore, creating surface has an energetic cost, reflected in the capillary term, which is also stabilizing.

From this expression an improved stability criterion, Eqs. (18) and (19), can be deduced (Sekerka 1965).

$$\left(\frac{\Delta H_m}{2\Lambda_l}+\frac{\nabla T_i^l}{v_i}\right) > -\frac{(\Lambda_s+\Lambda_l)}{2\Lambda_l} m_l \frac{c_i^l(1-k)}{D_l} S(A) \tag{18}$$

with:

$$A = -\frac{\Gamma k v_i}{m_l D_l (1-k) c_i^l} \tag{19}$$

This expression differs from Eq. (16) by taking into account a mean thermal conductivity and the latent heat of transformation but, more importantly, by the function $S(A)$, which takes into account the stabilizing effect of capillarity.

This function is plotted in Fig. 3.6. When $A = 1$, $S(A) = 0$ and the interface is stable. This occurs for high values of the interface velocity and will be discussed

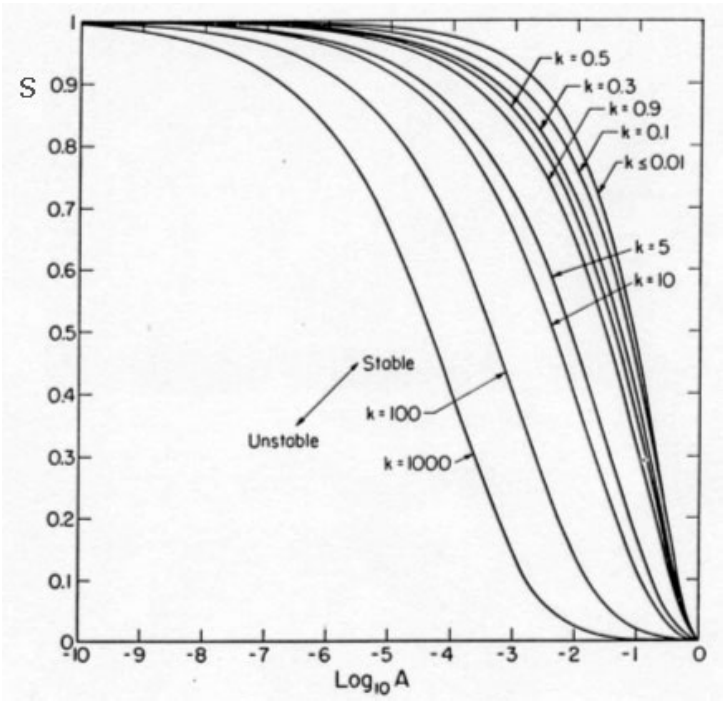

Fig. 3.6 Variation of Sekerka's stability function with the dimensionless parameter A (Sekerka, 1965).

in Section 3.2.3. At low growth rate, the latent heat term becomes negligible, $A \to 0$, $S(A) \to 1$, and the stability criterion takes a form similar to Eq. (16).

Finally, the periodicity of the fluctuation can be obtained by setting Eq. (17) equal to zero, which, for small growth rates, can be written as Eq. (20) (Kurz and Fischer 1998).

$$0 = m_l \nabla c - \nabla T - \Gamma \frac{4\pi^2}{\lambda^2} \tag{20}$$

Equation (21) follows.

$$\lambda = 2\pi \sqrt{\frac{\Gamma}{m_l \nabla c - \nabla T}} \tag{21}$$

It can be noted that λ takes a real value if Eq. (22) is true; this is the condition for instability already given in Eq. (16).

$$m_l \nabla c > \nabla T \tag{22}$$

For typical growth parameters used in metallurgy, the periodicity is of the order of 1 μm.

3.2.2 Dendrites

Destabilization of the interface leads to the formation of cell and dendrite structures. From the practical point of view, cells create defects in semiconductor crystals and crystal growers carefully avoid working under destabilizing conditions. Dendrites have been studied intensively in materials processing because they affect the properties of the alloy. This influence can be either negative (e.g., the disappearance of the transparency of silicate glasses in the case of dendrite generation within them), or positive (e.g., the increase in the elastic limit of eutectoid steels when the microstructure decreases in size).

The interface destabilization studied in Section 3.2.1 corresponds to the transition between Fig. 3.7(a) and (b). If the destabilization is increased (in this case by increasing the growth rate), the interface shows cells, then fully developed dendrites. The tips of the perturbations reject solute very efficiently and the regions between them trap solute, then grow more slowly. The resulting structure has a periodicity of its chemical composition, very often associated with precipitates or eutectics between the dendrites or cells.

It should be borne in mind that the structure obtained during solidification, close to the melting point, is likely to be significantly modified during the natural cooling of the solid, or during subsequent mechanical or thermal treatments. This modification depends on the alloy of interest: in the case of steels, the original structure of which can be totally lost after forging, whereas the solidification

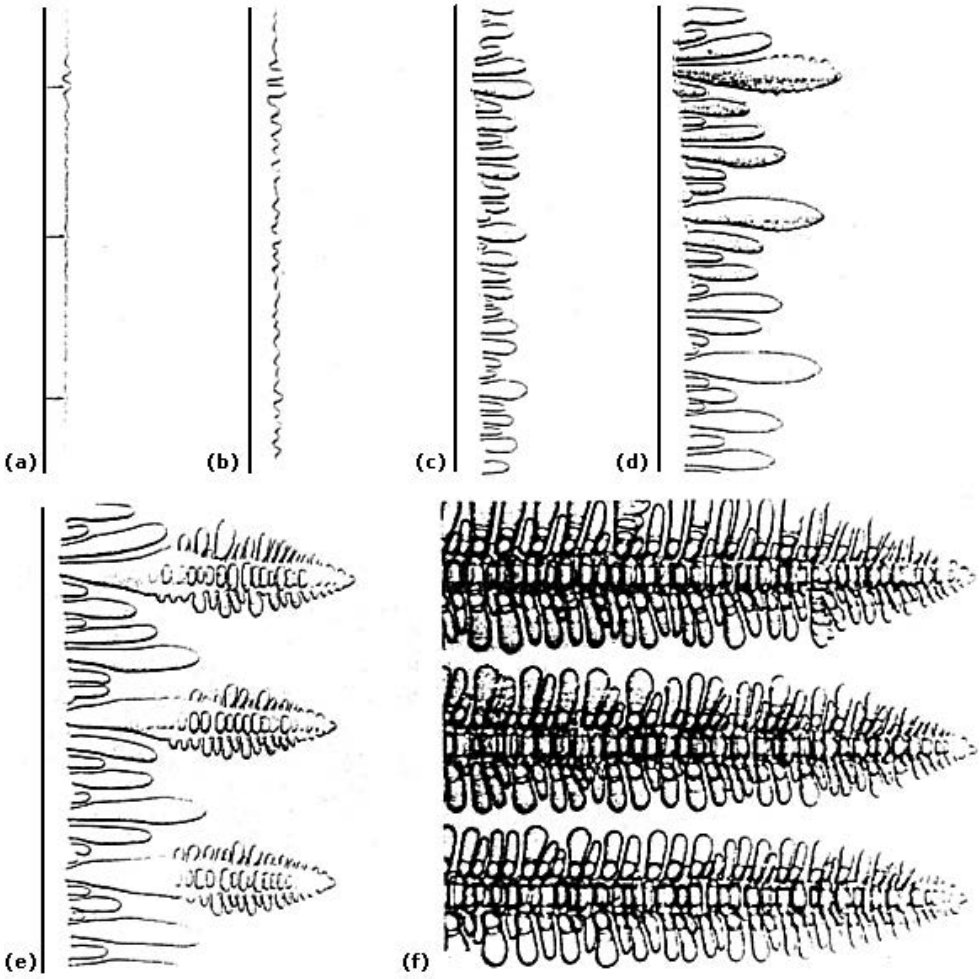

Fig. 3.7 From planar interface to dendrites: evolution of the solid–liquid interface structure when the growth rate is increased. The alloy is a transparent succinonitrile/acetone (4% mixture), solidified between two glass plates under a microscope. The liquid is on the right in all the pictures (Trivedi and Somboonsuk 1984).

structures in aluminum-based alloys do not change significantly during subsequent processes. These solid-state transformations are covered in Chapter 7.

3.2.2.1 **Different Types of Dendrites**

The dendrites obtained by destabilization of a macroscopic solid–liquid interface are called "columnar dendrites". They appear only in the case of an alloy processed under conditions of interface destabilization and their growth is con-

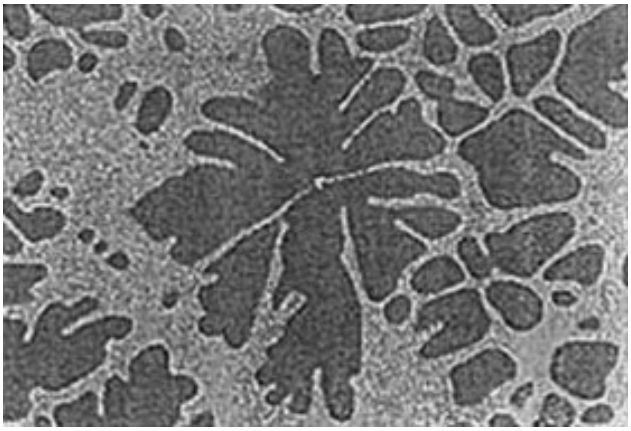

Fig. 3.8 Equiaxed dendrites in an Al–Ni alloy; each dendrite constitutes an individual grain (typical size 200 μm). The eutectic structure between the dendrites cannot be seen at this magnification.

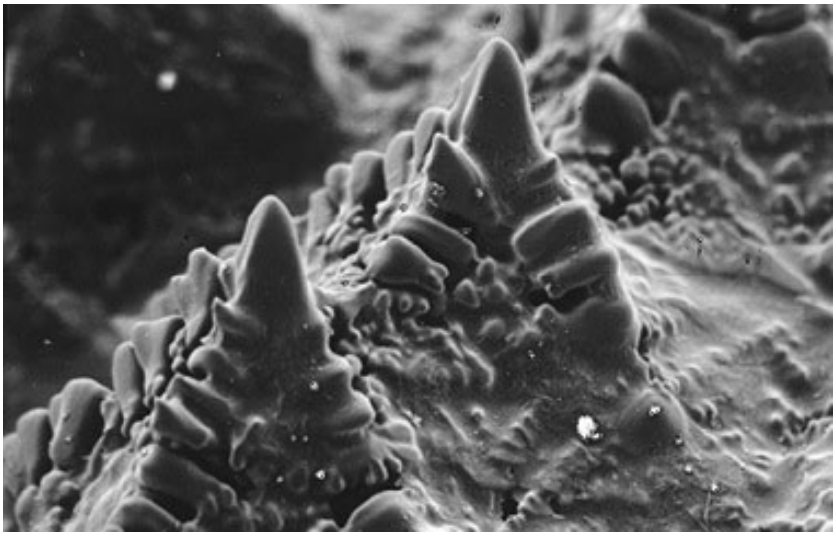

Fig. 3.9 Typical columnar dendrites in an Al–7%Si alloy: SEM observation of the interface after quickly removing the liquid. These dendrites have a typical size of 200 μm. Their faces are all oriented in the same direction, because they belong to the same single crystal grain (Access-Aachen).

strained (oriented) by the thermal gradient, so that the latent heat is evacuated by the solid. A common error is to associate structural grains with the dendrites. Generally speaking, the solid–liquid interface of a single grain is composed of several columnar dendrites: for example, single-crystal turbine blades are grown in the columnar dendritic mode.

Another type is called an ''equiaxed dendrite''. It is obtained when crystal seeds nucleate inside the liquid phase. This happens when the liquid is undercooled. Each seed grows on its own, at the beginning as a sphere, which may be maintained throughout the solidification (globular structures); more generally, however, dendrite arms appear on the crystal by destabilization. Growth is free (in all directions) and controlled by both solute and thermal diffusion into the liquid in the case of alloys. Equiaxed dendrites occur for pure elements as well, in which case the growth is controlled by thermal diffusion alone. Due to the release of latent heat, the solidified dendrite becomes warmer than the surrounding liquid and the latent heat is evacuated toward the liquid. Each equiaxed dendrite gives birth to an individual grain in the final structure.

Fig. 3.10 Shape of the columnar interface of an Al_2Cu intermetallic compound: SEM observation after quickly removing the liquid (Dupouy, 1986).

Fig. 3.11 Typical equiaxed carbon flakes in gray cast iron: optical metallography, typical size 500 μm.

The shape of the dendrite depends on the material. In the case of solid solutions based on simple crystalline metals with high symmetry (bcc, fcc) numerous growth directions are available and the structure shows an axis and secondary and even ternary arms typical of dendrites (Fig. 3.9). In general, the axis and the arms have simple crystallographic orientations, [001] in the case of cubic crystals, and the growth rate anisotropy is low.

In the case of intermetallic compounds with crystallographic structures of lower symetry, only a few growth directions are available; the dendrites are faceted and the growth rate anisotropy is high (Fig. 3.10).

Non metallic compounds have high melting entropies and they grow as thin plates, flakes, or needles (Fig. 3.11).

3.2.2.2 **Kinetics of Columnar Dendrites**

The fundamental hypothesis of all models for the study of dendrite dynamics considers that the growth is controlled by what happens at the tip of the dendrite. This rather surprising assumption (the dendrite tip radius is typically 1 μm and the dendrite length may be several hundreds of micrometers) is based on observations performed by Huang and Glicksman (1981) and Esaka (1986) and has been verified for the columnar dendrite.

For a given velocity, the problem is to find the most appropriate curvature of the dendrite tip to evacuate the amount of solute rejected. It is supposed that the solute field around the dendrite tip is purely diffusive. As shown in Fig. 3.12,

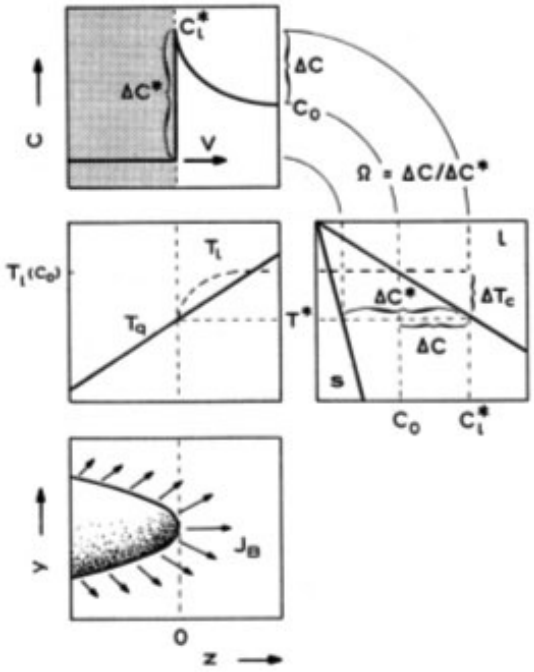

Fig. 3.12 Chemical and thermal fields in front of the tip of the dendrite (Kurz and Fischer 1998).

supersaturation and undercooling are related by Eq. (23) and depend on the chemical composition at the tip.

$$\Omega = \frac{c_i^l - c_0}{c_i^l(1-k)} = \frac{-\Delta T}{m_l k c_l^i} \tag{23}$$

It is therefore necessary to compute the solute field around the tip in order to solve the problem.

A parabolic shape of the dendrite is generally assumed and fits well with the observation of dendrites in transparent media in the diffusive approximation (see Fig. 3.13b).

The diffusion equation in this case has been solved by Ivantsov (1947) and gives Ivantsov's function Q [Eq. (24)].

$$\Omega = Iv(Pe) = e^{Pe} Pe \int_{Pe}^{\infty} \frac{e^{-z}}{z} dz \tag{24}$$

The leading parameter is the Peclet number, Pe [Eq. (25)].

$$Pe = \frac{v_i r}{2D_l} \tag{25}$$

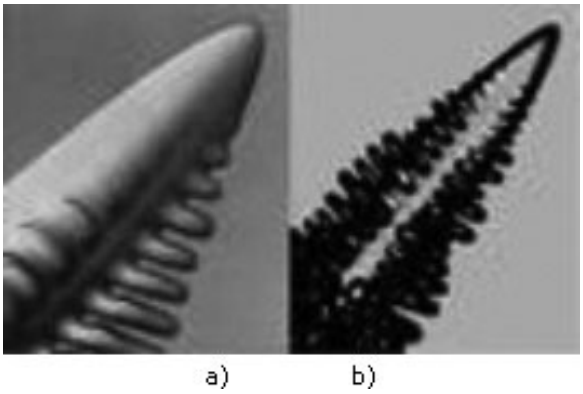

Fig. 3.13 Shape of succinonitrile dendrites: (a) under a liquid flow which is coming from the left and stabilizes the exposed side; (b) under microgravity conditions where no convection occurs (Huang and Glicksman 1981). Dendrite tip radius is a few μm.

If *Pe* is low (low growth rate), the supersaturation tends toward *Pe*, which is also the solution obtained by considering that the dendrite is a cylinder ending in a half-sphere, instead of a parabola.

This solution does not take into account the effect of capillarity, which has been added by Huang and Glicksman (1981). For example, in the low-*Pe* approximation, Eq. (24) is modified to Eq. (26).

$$\Omega = Pe + \frac{2\Gamma}{c_0 m_l (k-1) r} \tag{26}$$

The relationship imposed by Eq. (26) between tip radius and velocity at given undercooling is shown in Fig. 3.14, in which the Ivantsov solution is the straight line on the right-hand side and departure from this law under the effect of capillarity is seen to occur for small radii of curvature.

For a given supersaturation (undercooling in the thermal case) the number of couples (v_i, r) is practically infinite and another criterion is necessary to solve the problem. It was first considered that the tip radius is given by the extremum of the curve in Fig. 3.14, because it corresponds to the maximum velocity and minimum undercooling of the dendrite. However this leads to tip radii which are too small compared with the experimental values.

Langer and Müller-Krumbhaar (1977) have postulated that the tip radius is of the order of the periodicity of the interface destabilization. Their argument is that if the dendrite tip is smaller than this value the dendrite is likely to disappear, and if it is higher the dendrite tip will be destabilized and two dendrites will appear. From Eq. (21) we get Eq. (27), where the unknown variable is the solute gradient at the tip, which depends on the concentration at the interface.

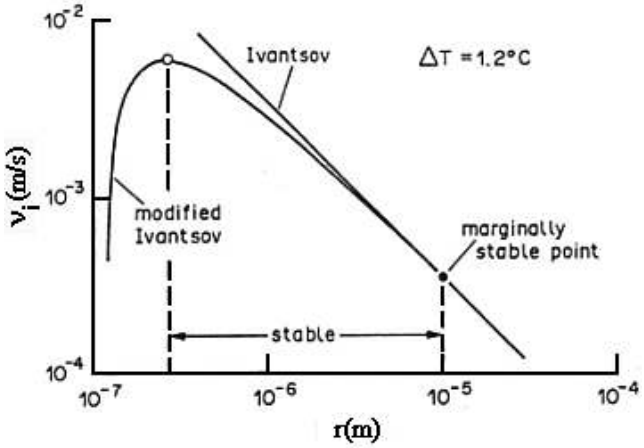

Fig. 3.14 Relationship between the velocity and the tip radius for a given undercooling/supersaturation (Kurz and Trivedi, 1990).

$$r = 2\pi\sqrt{\frac{\Gamma}{m_l \nabla c - \nabla T}} \tag{27}$$

Combination of Eqs. 8, 23, 26, and 27 gives a relationship between the growth rate and the tip radius which, in the case of a low growth rate and a negligible thermal gradient, can be written as Eq. (28) (Kurz and Fischer 1998).

$$r^2 v_i = 4\pi^2 \frac{D_l \Gamma}{c_0 m_l (k-1)} \tag{28}$$

This criterion is in good agreement with the dendrite tips measured by Glicksman.

3.2.2.3 Kinetics of Equiaxed Dendrites

For dendritic structures of pure metal growing in an undercooled melt (thermal equiaxed dendrites), the treatment of the columnar dendrite is applied, but the solute diffusion equation is replaced by the heat transfer equation, and Eq. (24) is replaced by Eq. (29).

$$\Delta T = \left(\frac{\Delta H_m}{C_p}\right) Iv(Pe) \tag{29}$$

The growth is not constrained, the velocity depends on the undercooling of the melt, and, in the simplified case of low *Pe*, the kinetic equations are (Kurz and Fischer, 1998) (30a) and (30b).

$$v_i = \frac{D_{th} C_p}{2\pi^2 \Delta H_m \Gamma} \Delta T^2 \tag{30a}$$

$$r = 4\pi^2 \frac{\Gamma}{\Delta T} \tag{31a}$$

In the case of an alloy, it is necessary to take into account simultaneously the thermal and the solute fields around the dendrite (Kurz and Fischer, 1998). This gives Eqs. (30b) and (31b).

$$v_i = \frac{D_l}{4 C_0 m_l (k-1) \Gamma} \Delta T^2 \tag{30b}$$

$$r = 4 \frac{\Gamma}{\Delta T} \tag{31b}$$

The equiaxed dendrite arms are very sensitive to sedimentation and convection, as shown by the comparison of experiments performed on Al–Ni alloys under microgravity (no sedimentation and convection), those under normal gravitational conditions (Dupouy and Camel, 2001), and those on transparent materials (Gerardin et al. 2001). Figure 3.15 shows the phase field simulation of the growth of an equiaxed dendrite in a liquid flow (phase field simulation techniques are

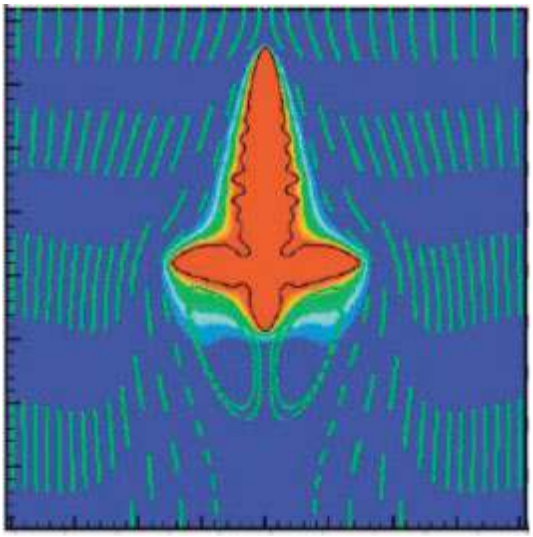

Fig. 3.15 Two-dimensional phase field simulation of free dendritic growth in a fluid flow. The flow enters at the top and leaves through the bottom. Colours indicate temperatures and the light lines are the streamlines (Boettinger et al. 2002).

discussed in Chapter 10). The dendrite arm facing the incoming liquid is accelerated, so that the equiaxed crystal becomes elongated in the direction of flow.

3.2.2.4 Characteristic Dimensions of the Dendrite

Knowing now the geometry of the dendrite tip, it is possible to compute the characteristic dimensions of the dendrite field: height, a, and periodicity, λ_1, under the hypothesis of an elliptical shape and regular hexagonal arrangement of the dendrite field. With a and b as half-major and -minor axis, respectively, the geometrical properties of the ellipse give Eq. (32).

$$r = \frac{b^2}{a} \tag{32}$$

Neglecting the tip undercooling, Eq. (33) follows from Fig. 3.16.

$$\lambda_1 = 1.7b = 1.7\sqrt{ra} = 1.7\sqrt{r\frac{\Delta T_0}{\nabla T}} \tag{33}$$

Substituting r from Eq. (28) gives λ_1 according to Eq. (34).

$$\lambda_1 = \frac{4.3}{\sqrt{\nabla T}}\sqrt[4]{\frac{D_l \Gamma c_0 m_l (k-1)}{k v_i}} \tag{34}$$

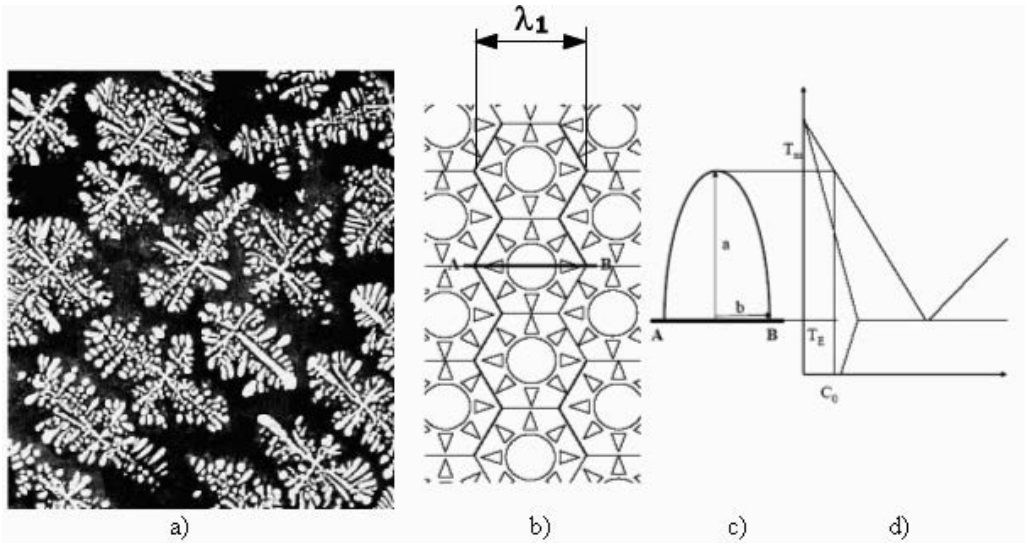

Fig. 3.16 (a) Columnar Al dendrites (0.5 mm diameter) in an Al–26wt%Cu alloy grown under microgravity in order to prevent convective perturbation (Dupouy et al. 1992); (b) their schematic representation as a hexagonal packing of ellipses; c) elevation along the line A–B; d) corresponding temperatures in the phase diagram.

Table 3.2 Experimental growth rate exponents for the primary spacing of dendritic arrays, for various alloys: $\lambda_1 \approx v_i^m \nabla T^n$.

Dendrite	Solute [wt%]	*m*	*n*
Al	2.2 to 10.1 Cu	−0.43	−0.44
	5.7 Cu	−0.36	–
	0.15 Mg, 0.33 Si, 0.63 Mg, 1.39 Si (at %)	−0.28	−0.55
	0.1 to 8.4 Si	−0.28	−0.55
	1 to 27 Cu	−0.5	−0.5
	1 to 5 Sn	−0.5	−0.5
	0.1 to 4.8 Ni	−0.5	−0.5
	5 Ag	−0.5	−0.5
Pb	2 to 7 Sb	−0.42	
	5 to 10 Sb	−0.75	−0.45
	10 to 50 Sn	−0.45	−0.33
	8 Au	−0.44	
	10 to 40 Sn	−0.39 to −0.43	−0.3 to −0.41
Fe	0.4 C, 1 Cr, 0.2 Mo	−0.2	−0.4
	8 Ni	−0.19	–
	0.6 to 1.5 C; 1.1 to 1.4 Mn	−0.25	−0.56
	0.035 C, 0.3 Si	−0.26	–

This parameter gives the main periodicity of the alloy structure and also of the defects that are generally trapped between the dendrites, precipitates, minority phases, microsegregations, and so on. Table 3.2 gives experimental values of the exponents of the growth rate and the thermal gradient, which are the principal process control parameters. It follows that Eq. (34) describes well the tendency but somewhat underestimates the effect of the growth rate.

Another important parameter is the secondary spacing, λ_2, which is the spacing between the secondary arms along the dendrite side. As follows from Figs 3.8 and 3.16(a), because of the evolution of the structure during cooling, these arms are degenerated and often are the only measurable structures. The original size of these arms, close to the dendrite tip, is the destabilization periodicity but, as can be seen from Fig. 3.13, it increases rapidly because of diffusion in the liquid between the arms, the solute going from the smaller arms toward the larger ones under the effect of capillarity (Ostwald ripening). This occurs as long as the sides of the dendrites are in contact with liquid. This phenomenon has been studied by Kattamis and Flemings (1965) and Feurer and Wunderlin (1977); they found an expression [Eq. (35)] for the spacing of secondary arms.

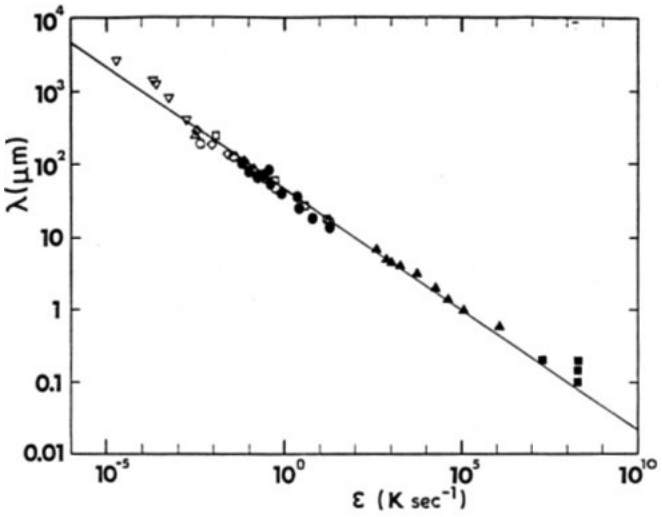

Fig. 3.17 Secondary spacing λ_2 as a function of cooling rate ε for Al–4%Cu and Al–11%Si alloys (Jones 1984).

$$\lambda_2 = 5.5\left(-\frac{\Gamma D_l \, ln\left(\frac{c_b}{c_0}\right)}{m_l(1-k)(c_b-c_0)}\,\frac{(T_0-T_b)}{v_i\nabla T}\right)^{1/3} \tag{35}$$

In Eq. (35) the subscript b stands for the bottom of the dendrite, often at the eutectic composition and temperature (as shown in Fig. 3.16d). This expression has been obtained with the help of crude hypothesis and simplifications, yet it gives a good description of the phenomenon and compares well with experimental observation (see Fig. 3.17).

3.2.2.5 **Microsegregation**

The cellular or dendritic morphology is the source of chemical heterogeneities in the material, as solute is trapped between the cells or dendrites and the composition varies periodically through the microstructure.

Equation (10) can be used to account for this periodic variation of solute, by considering the solidification of the dendrite thickness in the y direction, perpendicular to its z axis [Eq. (36)]. The tip of the dendrite solidifies at a composition close to the melt composition (Fig. 3.12) and solidification proceeds along a distance $\lambda_1/2$ till it reaches the side of the facing dendrite:

$$c(y) = kc_i^l\left(1-\frac{2y}{\lambda_1}\right)^{(k-1)} \tag{36}$$

When this concentration reaches the solubility limit, other solid phases precipitate, often as eutectic structures.

3.2.3 Rapid Solidification

The study of rapid solidification processes began in the 1960s, as it is a way to obtain materials in nonequilibrium and metastable states: microcrystalline or amorphous phases, such as metallic glasses. They are obtained by a rapid cooling of the sample, at 10^2–10^6 K s^{-1} (10^{11} K s^{-1} in certain laboratories). In this section the three major aspects of rapid solidification are explained: the stabilization of the solid–liquid interface, how it is possible to obtain metastable phases, and in which case an amorphous solid can be obtained. There are no direct relationships between these phenomena: amorphous and stable or metastable crystalline phases can be obtained below, as well as above, the absolute stability velocity.

3.2.3.1 Absolute Stability and Diffusionless Solidification

From Eqs. (18) and (19), it can be seen that, during directional solidification, the interface becomes unconditionally stable when the parameter A equals 1, which gives immediately the expression for the absolute stability velocity, Eq. (37).

$$v_a = -\frac{m_l D_l (1-k) C_0}{\Gamma k} \tag{37}$$

It is independent of the thermal gradient because its value becomes negligible compared with the solute gradient in front of the interface. With classical material parameters, the absolute velocity is in the range 0.1–1 m s^{-1}.

At very high growth rates, the solute boundary layer in the liquid decreases so much [Eq. (9)] that it becomes of the order of the interface thickness. Coming back to the argument developed in the Introduction [Eq. (2)] it follows that the interface velocity becomes so high that the atoms or molecules do not have enough time to rearrange at the interface and the liquid is solidified without any segregation; the solute segregation coefficient tends toward 1. Of course, the chemical potential of the solid and the liquid are no longer equal, as they are not in equilibrium. Aziz (1982) has proposed a relationship [Eq. (38)] for the velocity-dependent segregation coefficient:

$$k_v = \frac{k + \dfrac{a v_i}{D_s}}{1 + \dfrac{a v_i}{D_s}} \tag{38}$$

As k_v approaches 1 with increasing velocities, this favors the absolute stability of the front in the case of directional solidification. In the case of growth from the undercooled melt, dendrites become purely thermal once diffusionless solidification conditions are reached at the tip ($k_v = 1$).

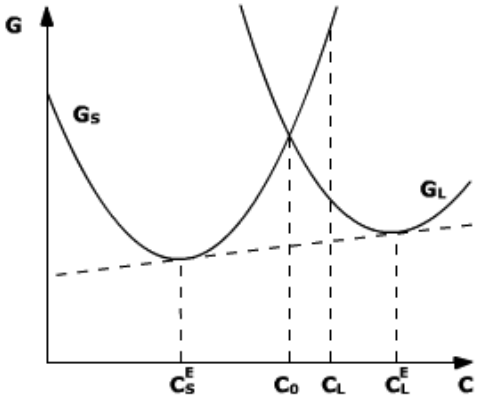

Fig. 3.18 Free energy of the solid and the liquid phases at equilibrium. The dotted line is a tangent to both energy curves corresponding to the solidus and liquidus lines ("double tangent construction").

In any case, the interface velocity cannot be higher than the velocity of sound in the liquid, which is of the order of 10^3 m s^{-1} for metals.

3.2.3.2 Nonequilibrium Phase Diagrams

An interesting fact in rapid solidification is that the undercooling of the interface increases with the growth rate (see Eqs. (5) and (6) for the kinetic effect, or Eqs. (23)–(25) for a columnar dendrite) and liquids can be solidified far from their equilibrium melting temperature, in regions of the phase diagram where metastable phases can be obtained.

At equilibrium, for a given temperature T, the compositions of the solid and liquid phases are defined through the free energy diagram (Fig. 3.18) (see Chapter 7 for calculation of phase diagrams).

When rapid solidification occurs, the chemical compositions of the solid and of the liquid can be equal, as explained above, but they cannot be higher than c_0, otherwise the energy of the solid would be higher than the energy of the liquid. Therefore, for the given temperature T, it is possible to get a solid with compositions ranging from c_e to c_0. The corresponding T–c_0 curve, known as the T_0 line, can be plotted in the phase diagram of the alloy, as shown in Fig. 3.19. It is located between the liquidus and solidus lines.

Provided that the undercooling is large enough, it can be seen from Fig. 3.19 that the composition domain of the equilibrium phases can be increased. But the most important application is that other phases, which cannot be solidified at equilibrium, can be obtained.

3.2.3.3 Structure of the Rapidly Solidified Phase

Crystals show well-ordered piles of atoms. On the contrary, amorphous solids, such as glasses, show atomic arrangements that are closer to the structure of

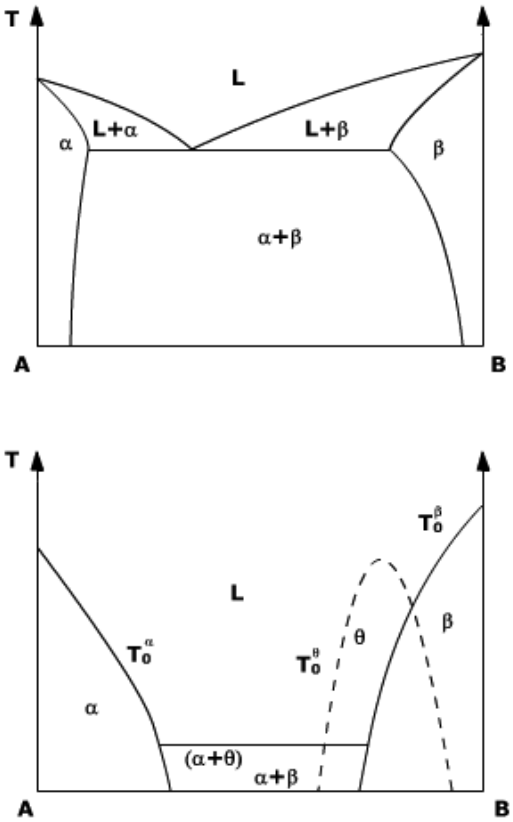

Fig. 3.19 Comparison between the equilibrium and the kinetic phase diagram of a given alloy. The eutectic temperature is substantially lowered, the eutectic composition width decreases, and a new solid phase θ appears.

liquid phases, with absence of topological long-range order. Obtaining one or the other structure depends on the probability of nucleation of crystal seeds in the cooling liquid.

The nucleation rate of seed crystals depends on two factors. In order to nucleate, a seed should be large enough, so that enough solid is created to counterbalance the energy cost of creating the seed surface. Once the seed has nucleated, it should be fed by diffusion through the liquid in order to grow. Both mechanisms are energetically activated and the nucleation rate, i.e., the number of growing seeds nucleated per second, is given by Eq. (39), with ΔG_n depending on the undercooling of the liquid according to Eq. (40) (see Chapter 7 for a detailed discussion of the nucleation mechanisms).

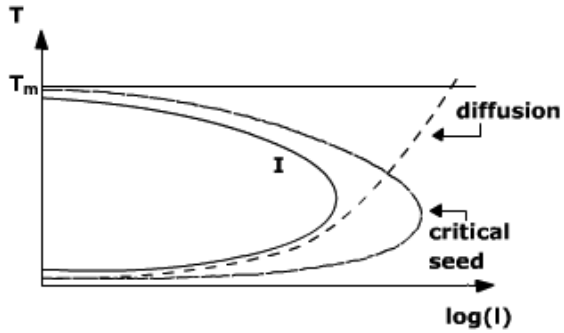

Fig. 3.20 Evolution of nucleation rate below the melting temperature.

$$I = I_0 e^{-\Delta G_n/k_B T} e^{-\Delta G_D/k_B T} \tag{39}$$

$$\Delta G_n = \frac{16\pi}{3} \frac{\gamma_{sl}\Gamma^2}{\Delta T^2} \tag{40}$$

Figure 3.20 shows both contributions and the corresponding nucleation rate.

In general, this curve is presented in a plot of temperature versus time; see Fig. 3.21 (known as a TTT diagram, for Time–Temperature–Transformation), where the curve gives the time after which a given nucleus density or solid fraction is obtained.

Three domains can be distinguished in this diagram. Above the melting temperature, the sample is liquid. Below the melting temperature, the crystalline phase is obtained in the domain on the right of the ''nose''-shaped curve. In the case of a small undercooling, the time to obtain the first crystal seed may be very long (path 1). When the undercooling increases, the probability of seed nucleation increases as well and the critical nucleus size decreases. However, after pass-

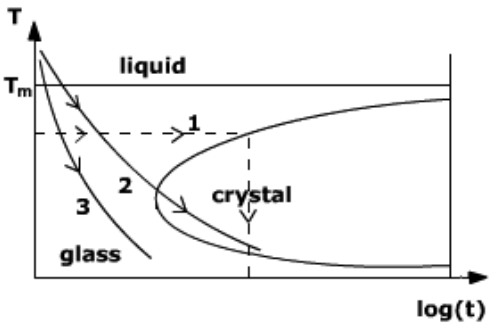

Fig. 3.21 TTT diagram, showing how the cooling rate selects either the crystalline or the amorphous structure of an alloy.

ing a certain critical undercooling, it becomes difficult to get crystals because the nucleation and diffusion processes are both thermally activated.

It follows from this diagram that, whatever the material or alloy, there always exist cooling conditions permitting either the crystalline (path 2) or the amorphous (path 3) phase to be obtained. However, the critical cooling rate to get crystals may be extremely low for materials such as silica glasses. On the contrary, extremely high cooling rates, of the order of 10^6 K s^{-1} and obtainable only on thin materials (ribbons, wires and suchlike), are usually necessary to get amorphous metallic binary alloys. In practice, the difficulty of obtaining a crystal seed increases with the complexity of the crystallographic structure, which in turn increases with the number of different atoms in the structure. It follows that it is easier to get metallic glasses of quaternary or quinary alloys: centimetric bulk metallic glasses of Zr–Ti–Ni–Cu–Be are currently produced with cooling rates of the order of 10 K s^{-1} (Johnson 1999).

3.2.4
Eutectic Structures

Eutectic structures occur when two or more solid phases grow simultaneously from the liquid. This generally leads to tiny structures, of the order of 1 μm. Eutectics are composite materials and often show very good mechanical properties.

3.2.4.1 Size of the Eutectic Structure

The derivation of the period of a eutectic structure has been introduced by Jackson and Hunt (1966). The calculation presented here is a simplified version for a symmetric phase diagram and equivalent physical parameters of both phases, together with linearized fluxes.

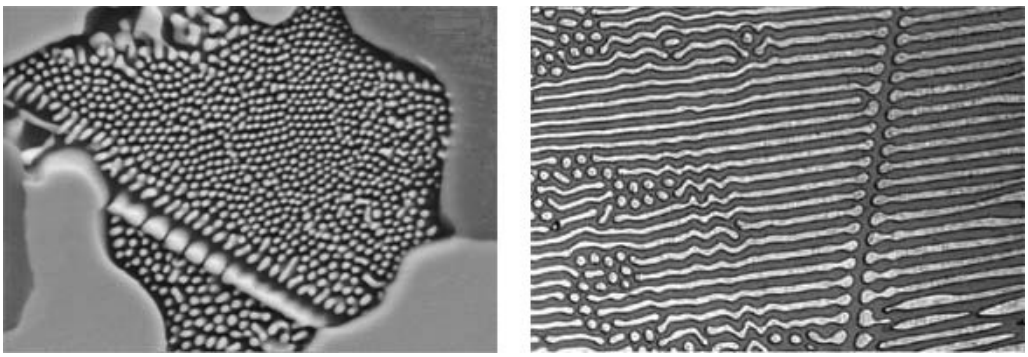

Fig. 3.22 Typical fibrous (Ag_2Al phase in a Cu–Zn–Al–Ag alloy) and lamellar (Al–23%Cu alloy) eutectic structures. Their characteristic dimension is 1 μm (Access-Aachen).

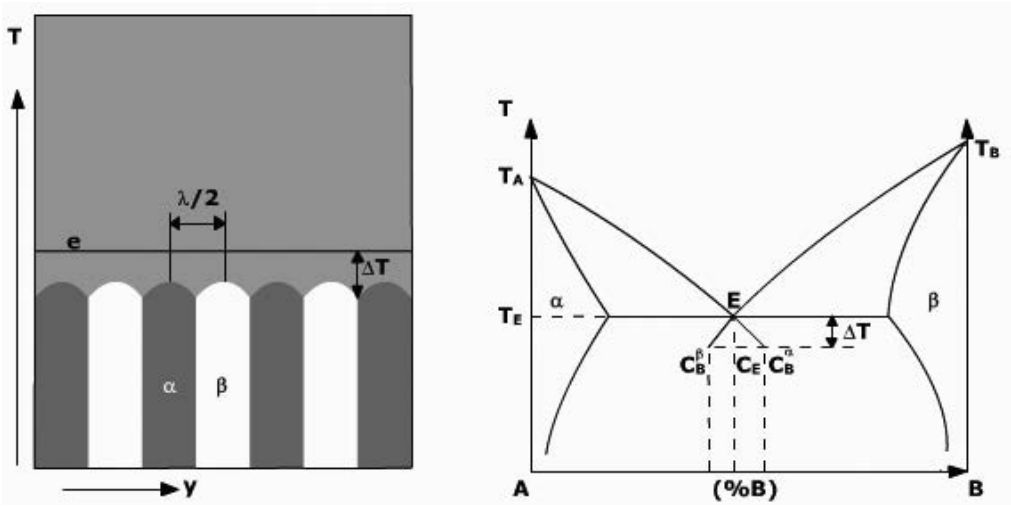

Fig. 3.23 Lamellar eutectic growth and corresponding phase diagram.

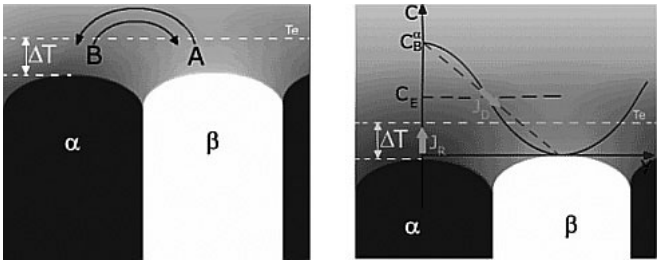

Fig. 3.24 Diffusion of solute rejected by one phase in order to feed the adjacent one.

Each phase rejects the solute corresponding to the growth of the other phase, which then will diffuse in order to feed the adjacent lamella (Fig. 3.24).

In a first approximation, the flux of B atoms from the α to the β phase can be written as Eq. (41).

$$J_B = -D_l \frac{(C_B^\alpha - C_B^\beta)}{\frac{\lambda}{2}} \tag{41}$$

From [Eq. (8)], the flux of solute B rejected by the α phase is given by Eq. (42).

$$J_B = v_i c_B^\alpha (1 - k) \tag{42}$$

Under conditions of stationary growth, both fluxes are equal and the composition is close to the eutectic composition, which gives Eq. (43).

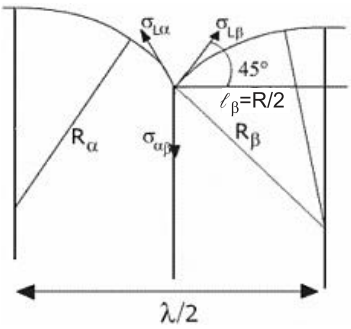

Fig. 3.25 Geometry of a junction of two lamellae with the equilibrium of the surface energies leading to the curvature of the solid–liquid interface at the lamella top.

$$(C_B^{\alpha} - C_B^{\beta}) = \frac{\lambda v_i c_E (1-k)}{2D} \tag{43}$$

Equation (44) is the corresponding expression in terms of chemical undercooling (see Fig. 3.23).

$$\Delta T_{ch} = \frac{c_E(1-k)}{2D\left(\frac{1}{m_\beta} - \frac{1}{m_\alpha}\right)} \lambda v_i \tag{44}$$

The geometry of the junction between two lamellae gives another expression [Eq. (45), derived from Eq. (13)] for the undercooling (Fig. 3.25). It is supposed that the top of the lamella is a portion of a circle and that the geometry is symmetric.

$$\Delta T_{cap} = \frac{2\Gamma}{\lambda} \tag{45}$$

The temperature of the eutectic interface T_i is plotted in Fig. 3.26 with the two undercooling terms ΔT_{ch} and ΔT_{cap} [Eq. (46)].

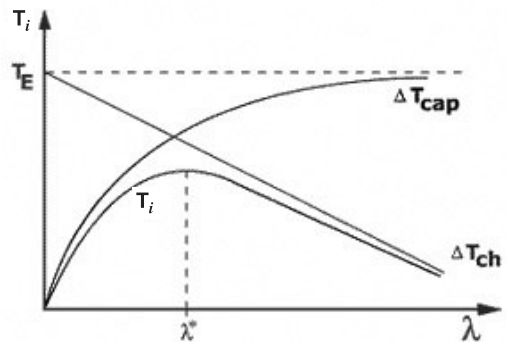

Fig. 3.26 Temperature of the eutectic interface versus eutectic spacing.

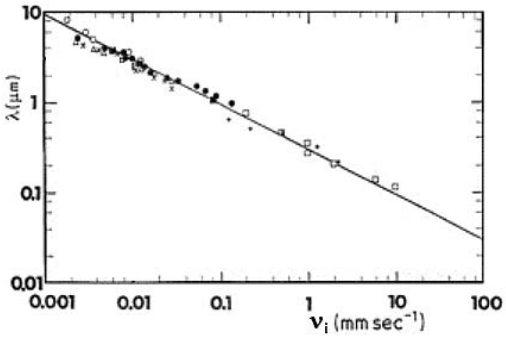

Fig. 3.27 Variation of the eutectic spacing with the growth rate for the Al–Al_2Cu eutectic (Jones 1984).

$$T_i = T_E - \Delta T_{ch} - \Delta T_{cap} \tag{46}$$

The system is likely to adopt the position where the energy, and thus the undercooling, are minimal.

The eutectic spacing is then obtained by derivation of Eq. (46) with respect to λ and finally gives Eq. (47).

$$\lambda^2 v_i = 4 \frac{D\Gamma\left(\frac{1}{m_\beta} - \frac{1}{m_\alpha}\right)}{c_E(1-k)} \tag{47}$$

This simplified relationship captures the basic physical concepts leading to the eutectic spacing: the periodicity of the structure is a compromise between the interdiffusion of the species, which works better when the distance between lamellae is decreased, and the surface energy, which tends to increase the thickness of the lamellae. It should be noted that in a first approximation the thermal gradient and the alloy composition have no effect on the eutectic structure. Equation (47) is in good agreement with results for an Al–Al_2Cu eutectic (compare Fig. 3.27).

3.3
Defects in Single and Polycrystals

Section 3.2 has reviewed the main theories developed in order to explain the structures obtained after solidification. However, the reality is generally more complicated and materials and structures are not as ideal and perfect as could be expected from the previous explanations.

This section is therefore devoted to analysis of the defects which are generated during the solidification of alloys. This applies essentially to two classes of alloys and growth regimes: single crystals, which are expected to have a highly perfect atom arrangement, and dendritic structures, because perturbations of the den-

dritic field are likely to create defects in the material which may cause the mechanical properties of the alloy to deteriorate and restrict considerably its technical application. Section 3.3.2 is devoted to the development of the grain structure of an alloy.

3.3.1 Defects in Single Crystals

A convenient way to classify defects is to use their characteristic dimension.

3.3.1.1 Point Defects

A full treatment of point defects, such as vacancies, interstitials, antisites and so on, is provided in Chapter 5.

Solidification by itself has no direct effect on point defects in pure elements. As the liquid phase is not constrained and electrically neutral, the basic principle is that the interface acts as an ideal source and sink of point defects that are incorporated in the solid at their equilibrium value, which depends essentially on the temperature. Considering Si at its melting temperature, vacancies and interstitials show a level of 10^{15} cm^{-3} in the solid, while holes and electrons are at the 10^{19} cm^{-3} level. However, only a rough interface is an ideal surface, faceted interfaces may decrease the level of defects because the energy of one atom absorbed on or desorbed from the interface is high in this case.

The situation is more complicated in compound phases. For GaAs, vacancies and interstitials are at the level of 10^{19} cm^{-3} (0.05%) for a perfectly stoichiometry and neutral material, but it is difficult to obtain stoichiometry. Figure 3.28 shows an enlarged view of the phase diagram of GaAs. It appears that the congruent point is shifted to the As-rich side, which means that only $Ga_{0.497}As_{0.503}$ can be grown without segregation effects. However, during cooling, this will cause As to precipitate. The situation is complicated by the fact that As has a high vapor pressure above liquid GaAs (2 atm at the melting point). Perfectly stoichiometric GaAs can be grown from the liquid phase, provided that its composition is controlled continuously during growth, which is technically (but not easily) obtained by controlling the As pressure in the gas in equilibrium with the liquid.

In turn, antisite defects (for definition and more details, see Chapter 5) are controlled by the stoichiometry of the compound. An important defect in GaAs, known as *EL2*, is As_{Ga}. The reaction governing this defect is represented by (Lagowski et al. 1982):

$$As_{As}{}^{0} + h_{Ga}{}^{-} \rightarrow As_{Ga}{}^{2+} + h_{As}{}^{+} + 4e^{-}$$

It is found that the concentration of *EL2* is dependent on stoichiometry, but also on the electrical state of the semiconductor [Eq. (48)].

$$[As_{Ga}] = K(T)\frac{[h_{Ga}]}{[h_{As}][e^{-}]^{4}} \tag{48}$$

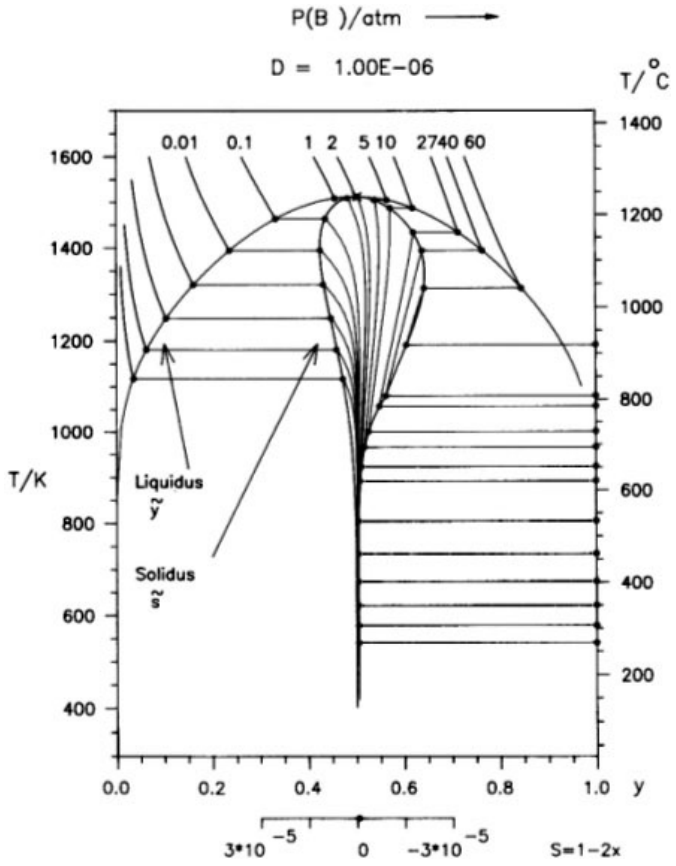

Fig. 3.28 GaAs phase diagram with an enlarged view of the solidus close to the stoichiometric point superposed on it (Wenzl et al. 1991).

1D: Dislocations Dislocations are covered in detail in Chapter 6, and only a few comments on their interaction with solidification will be given here.

The only stress applied on the growing solid–liquid interface is the hydrostatic pressure. For materials which are very soft at the melting temperature, for example, HgI_2, this may have an effect on the dislocations created in the crystal. However, this pressure is negligible in more conventional materials and a no-stress mechanical boundary condition is typically used on the interface. It follows that the solidification process by itself does not generate dislocations.

Stresses occurring after solidification, during the cooling process, or because of possible adhesion on crucible walls easily generate dislocations in the crystal; especially close to the melting point where plasticity is enhanced (Gondet et al. 2003). Since this process is not directly linked to solidification matters, it will not be covered here, but the reader should be aware that it is the main cause of dislocation generation in industrial single crystals (see Völkl, 1994).

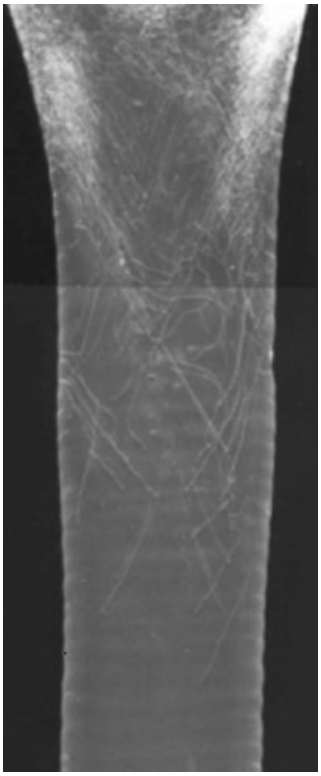

Fig. 3.29 X-ray topography of the seed of a zone-melting Si single crystal. Dislocations appear as white lines and their number decreases as growth proceeds, from top to bottom (Hurle and Rudolph 2004).

Solidification may be used to decrease the number of dislocations in crystals. If dislocation lines are not perfectly perpendicular to the growing interface, they will move, as growth proceeds, toward the edge of the crystal, where they will disappear. This property is used for ''cleaning'' seeds in the pulling of Si single crystals (Fig. 3.29) (Dash 1959).

Last but not least, the reader should keep in mind, as mentioned in the Introduction, that the existence of dislocations at the growing interface has a strong effect on the undercooling, especially in the case of faceted growth.

2D: Twins and grain boundaries Although point defects and dislocations can, to a certain extent, be accepted in single-crystal production, this is not the case for twins and grain boundaries which separate the sample into two or more parts with different crystallographic orientations, making the material unsuitable for a use as single crystal.

It is well known that twins and grains are easily produced during mechanical deformation of materials (see Chapter 6). The thermal stresses occurring during the cooling phase of crystal growth processes are not large enough to produce twins, but they produce dislocations that may align in sub-grain boundaries and, ultimately, give grains (Boiton et al. 1999). Since this is not directly linked to

solidification it will not be discussed further here (for a discussion of thermal stresses in crystal growth, see Völkl, 1994).

3.3.1.2 **Twins**

Twins are specifically linked to single crystals, because they are due to a defect in the stacking of atom piles, leading to a rotation of the crystal structure (Fig. 3.30). The energy associated with the twin plane is due to the stacking faults and is relatively low compared with a grain boundary, so that twins can grow easily under certain conditions.

The twinning of a crystal during Czochralski pulling will be discussed, but the case can be extended to other crystal growth processes where a crucible wall is in contact with both liquid and solid. A first condition for the twinning to occur is that the solid–liquid interface is faceted at the crystal–liquid–gas triple line (Fig. 3.31). It can be shown that a twinned seed cannot nucleate in the middle of the facet, because its energy, increased by the twin energy boundary, is higher than the energy of a regular seed.

Hurle (1995) has shown that twinning will occur on the facet at the triple line, if a twinned seed can nucleate. Such a seed is a truncated disk and its energy is lower than for a regular, circular, seed. The question is under which conditions a truncated twinned seed has a lower energy than a truncated regular (well-oriented) seed. The key point is that the lateral surface of the seed (facing the gas) should have a given orientation, generally $\langle 111 \rangle$. This happens if the angle α in Fig. 3.31 is 70.5°, which is likely to occur in the conical part of the crystal, when its diameter is increased. Temperature oscillations, leading to diameter fluctuations, are also a cause of reaching this particular value.

In order to make possible the growth of the twinned seed, it should also be small enough; this gives a value for its undercooling according to Eq. (49), where subscripts *TB*, *C* and *T* respectively stand for the Twin Boundary, for a Circular seed, and for the Truncated seed.

$$\Delta T_s = \frac{\gamma_{TB}}{a\Delta S_m} \frac{\Delta G_C}{\Delta G_C - \Delta G_T} \tag{49}$$

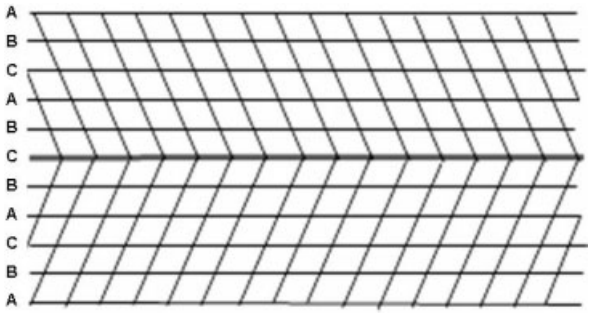

Fig. 3.30 Typical twin boundary, due to an error of piling A, B, and C atomic planes.

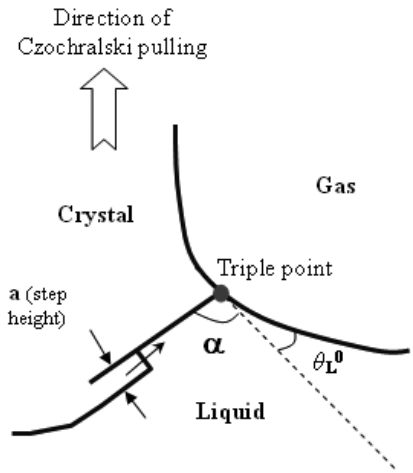

Fig. 3.31 Normal growth in the Czochralski process: the facet at the triple line grows step by step. A twin may occur if a seed of this orientation nucleates at the triple line.

It follows that the facet on which the twinned seed is nucleating should be highly undercooled. As dislocations facilitate the growth of faceted crystals and then decrease their undercooling, twins are more likely to appear in crystals with a very low dislocation density, which is in good agreement with the experimental observation.

3.3.1.3 **Grains**

Single-crystal growth often fails because the occurrence of grains. Due to the energy associated with the grain boundary, the nucleation of a randomly disoriented seed directly on the growing interface is not possible and the mechanism should be different from that of twin nucleation. The basic principle is still the decrease in energy of the seed of a grain with respect to a seed correctly oriented on the interface. This may occur if foreign surfaces, on which a disoriented seed can grow, are present in the system. Such surfaces are typically precipitates or crucible walls. In addition, the grain seed should nucleate ahead of the interface and then a certain undercooling is necessary.

As shown in Fig. 3.32, two configurations may lead to grain nucleation in the layer of undercooled melt ahead of the interface: nucleation on a crucible wall, and in holes of a rough crucible. Only the case of a seed nucleating on the crucible wall (Duffar et al. 1999) will be discussed here, but the treatment of the other configuration is equivalent. In processes without crucibles, grains nucleate on foreign particles or on precipitates in the melt.

From the nucleation theory, there is a critical radius for nucleation of a 2D nucleus on a faceted interface [see Eq. (12)] and the associated energy is given by Eq. (50).

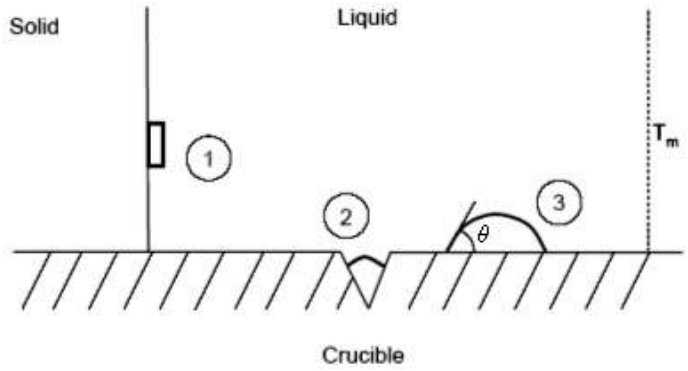

Fig. 3.32 Nucleation of solid seeds: (1) on the interface; (2) in a hole in a rough crucible. (3) Spurious nucleation on the crucible wall.

$$\Delta G_I = \frac{\pi a \gamma_{sl}^2}{\Delta S_m \Delta T} \tag{50}$$

On the crucible wall, the critical seed has a similar radius, but the energy is decreased by a factor depending on the contact angle of the seed on the wall [Eq. (51)].

$$\Delta G_W = \frac{16\pi\gamma_{sl}^3}{3\Delta S_m{}^2 \Delta T^2} \frac{(2 + cos\,\theta)(1 - cos\,\theta)^2}{4} \tag{51}$$

Figure 3.33 shows that if the contact angle is low enough, spurious nucleation may occur, even for low values of undercooling.

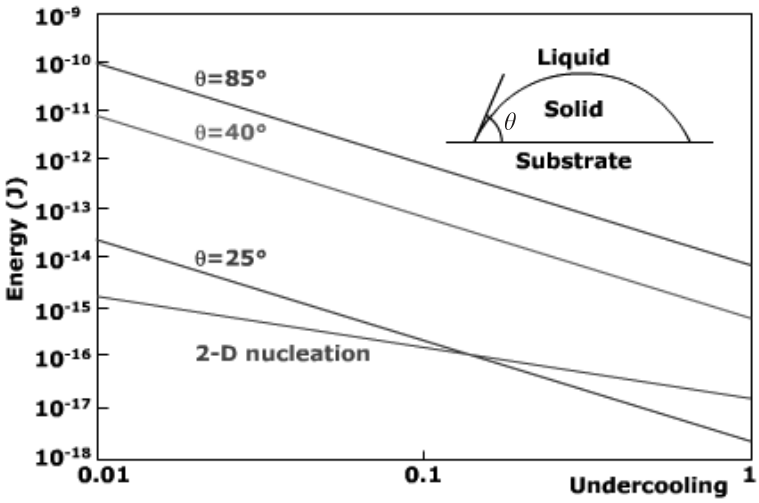

Fig. 3.33 Nucleation energy of a 2D nucleus on the interface and on walls with various contact angles, plotted as a function of the undercooling.

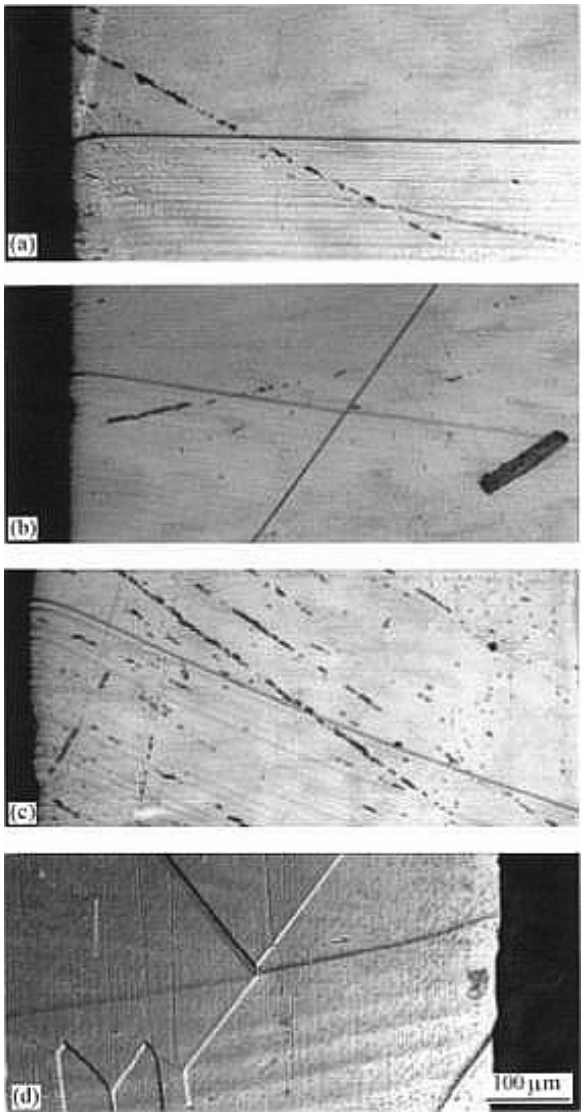

Fig. 3.34 Metallographs of marked GaSb solid–liquid interfaces, in contact with the crucible wall: (a) silica ($\theta = 100°$); (b) vitreous carbon ($\theta = 90°$); (c) BN with carbon coating ($\theta = 90°$); (d) BN ($\theta = 40°$, the crucible wall is on the right).

Figure 3.34 shows the angle made by a solid–liquid interface on a crucible wall. The measured angles, introduced into Eq. (51), are in agreement with the observation that spurious nucleation in GaSb crystal growth never occurs in silica crucibles, but always happens in BN crucibles.

3.3.2
Grain Structure of an Alloy

As already mentioned in Section 3.2.2 with respect to dendrites, the grain structure of an alloy is of primary importance to its mechanical properties. Grain boundaries are defect zones with a high energy (0.5 J m^{-2}, close to the energy of a solid–liquid interface), attracting stresses and impurities, and helping the precipitation of foreign phases. On the one hand, this results in a cleaning effect of the intragranular material but, on the other hand, grain boundaries may be locations of corrosion, mechanical weakness, or crack initiation. Although this is extremely alloy-dependent, it is generally recognized that the quality of an alloy is improved when grains are smaller.

Grains can be columnar, when they are elongated in the direction of the growth, and in this case each grain is constituted by several columnar dendrites (see Section 3.2.2). Grains with an isotropic shape are called equiaxed and they are generally produced from individual equiaxed dendrites. As shown on Fig. 3.35, it is possible to change the growth conditions in order to get one or the other type of grain structure.

Typical defects are associated with the grain structure.

- Chemical segregation may occur between dendrites and grains, and on the full ingot scale. Precipitation of oxides, sulfides, or eutectic phases, or nucleation of dissolved gases (H_2) often follows.
- Shrinkage may also occur between dendrites and grains, and on the ingot scale. It is a major defect that deserves much attention. Its distribution across the solid depends strongly on the solidification conditions.

Fig. 3.35 Transition from columnar (left) to equiaxed (right) grain growth through an increase in the growth rate from 2 to 15 μm s^{-1} (refined Al–3.5%wtNi, $\nabla T = 20$ K cm^{-1}) (Dupouy and Camel 2000). Diameter 8 mm.

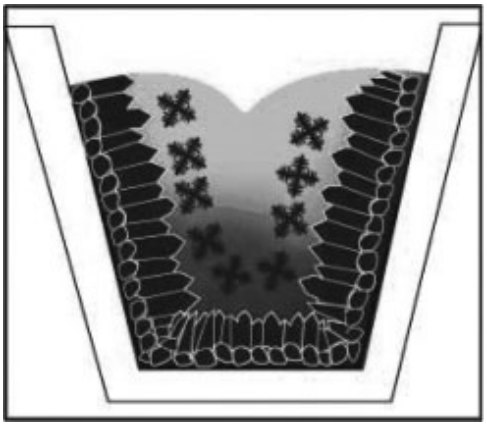

Fig. 3.36 Typical grain structure in a cast alloy.

In practice, all metallurgical processes consist in pouring the liquid into a mold. The extraction of heat toward the walls leads to a typical grain structure in the cast ingot which is shown in Fig. 3.36. There are three zones: the outer dendrites, the columnar region, and an equiaxed area in the center.

The outer equiaxed zone is composed of small grains that grew by heterogeneous nucleation in the undercooled liquid at the mold walls (step 1; compare Fig. 3.37). As there is a great heat extraction by the mold, their growth rate is

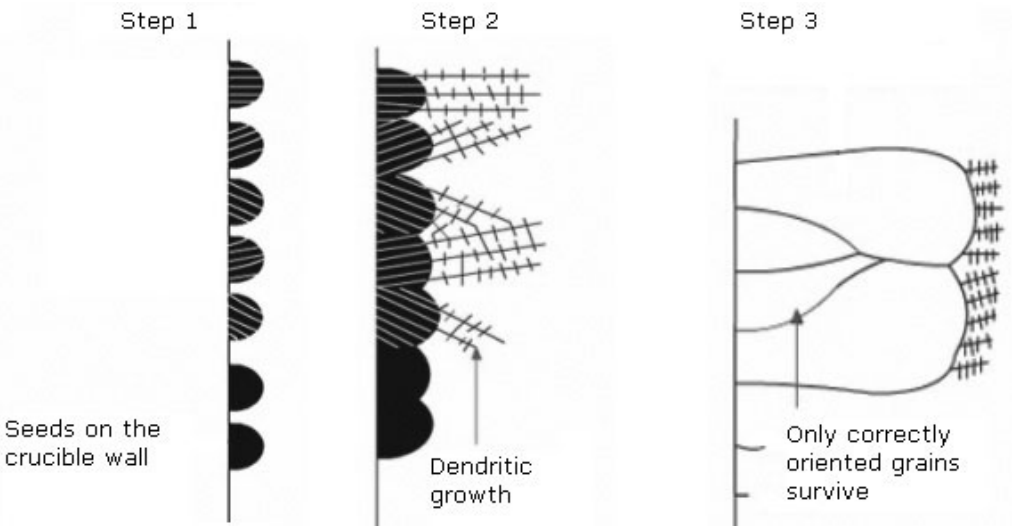

Fig. 3.37 Three steps of the transition from the outer equiaxed zone to the columnar structure.

Fig. 3.38 Grain structure of an alloy as predicted by Gandin's stochastic model (Gandin and Rappaz, 1994). The growth proceeds from the left to the right and the effect of melt convection can be seen. The colors are representations of the various crystallographic orientations of the grains.

high and destabilization occurs, leading to columnar dendritic growth (step 2). Dendrites follow the crystallographic orientation of the initial grain and those oriented opposite to the thermal flux "overgrow" the others, so that grain selection occurs (step 3).

So far, these nucleation, growth, and grain selection mechanisms have been modeled only through stochastic numerical simulation, with realistic and predictive results (Fig. 3.38). The method and some results are given in Rappaz and Gandin (1993) and Gandin and Rappaz (1994).

The central equiaxed region appears when the thermal gradient in the liquid vanishes and seeds transported from the front (detached dendrite arms) are able to grow in the liquid. Depending on the application of the alloy, it is possible to avoid the equiaxed structure (photovoltaic silicon, turbine blades) or on the contrary to favor it, by mixing the liquid or using refining particles.

In Section 3.3.2.1 the equiaxed grain growth regime is studied, in an attempt to find out the typical size of the grain structure. The parameters involved in the columnar to equiaxed transition are explained in Section 3.3.2.2.

3.3.2.1 Equiaxed Growth in Presence of Refining Particles

Grain refining is used to get a homogeneous and tiny equiaxed structure. It consists in enhancing the heterogeneous grain nucleation with the help of foreign solid particles introduced in the melt. The principle is based on the fact that heterogeneous nucleation on foreign particles is easier than homogeneous nucleation, especially if the contact angle of the seed on the particle is low [Eq. (51)].

The first condition is to have nucleating particles (refiners) in the melt. Finding adequate particles is not easy because they should not dissolve in the melt and

they should have nucleation properties only for a sufficiently undercooled melt. In practice, two refinement processes are used (Jackson et al. 1966).

- Introduction of the appropriate particles in an undercooled melt. A very typical example is the introduction of Ti (1–10%) and B (0.1–3%) in Al alloys.
- Strong mixing of the melt, for example by electromagnetic forces. The common assumption is that the melt flow is strong enough to detach secondary arms of columnar dendrites (this detachment occurs by chemical dissolution rather than mechanical effect) and these solid particles are seeds for the equiaxed growth if they remain in or pass into an undercooled liquid.

The second condition means that the melt should be, and should remain, undercooled as long as possible. However, because of the equiaxed dendrite growth, latent heat is released in the system and the liquid temperature increases. It is only in the case of efficient solute rejection by the grains that the liquid remains undercooled (chemical undercooling, Eq. (3)) and that the growth of the already existing grains is restricted. This ability is measured by the parameter of growth restriction, q [Eq. (52)].

$$q = m_l(k-1)c_0 = k\Delta T_0 \tag{52}$$

The number of grains in the alloy is a direct consequence of the competition between the heterogeneous nucleation rate, which increases with the undercooling, and the growth rate, which decreases as the undercooling increases.

In the model proposed by Maxwell and Helawell (1975), three different regimes are considered.

In a first step, the hot liquid cools down, passes the melting temperature, then is undercooled. The energy barrier for nucleation of a seed on a foreign particle is given by Eq. (51) and therefore decreases when the undercooling increases and nucleation starts at a given undercooling. The nucleation rate is given by Eq. (39) and is proportional to the number of foreign particles N_p. Considering the low undercooling, the diffusion term is taken to be constant and Eq. (53) results.

$$\frac{dN}{dt} = N_p I_0 e^{-\Delta G_n/k_B T} \tag{53}$$

In the second step, particles are growing. It is supposed that the undercooled liquid is isothermal and that the solute fields around the particles are not interacting, so that the liquid between two grains is at the initial composition. These assumptions are based on the fact that the thermal diffusivity is two to three orders of magnitude higher than the chemical diffusivity. Then the characteristic length for chemical diffusion is smaller than the typical grain size (200 μm) but the characteristic length for the heat transport corresponds to hundreds of grains.

The crystals are spherical and their growth rate is limited by the solute rejection and then varies inversely with q. The time evolution of the radius of a particle growing and rejecting solute has been obtained by Aaron et al. (1970) as Eqs. (54).

$$
\begin{aligned}
r &= \lambda\sqrt{D_l t} \\
\lambda &= \sqrt{\frac{S^2}{4\pi} - S} - \frac{S}{\sqrt{2\pi}} \\
S &= -\frac{2\Delta T_S}{m_l(k-1)(C_0 - \Delta T_S/m_l)}, \quad \Delta T_S = m_l(c_i^l - c_0)
\end{aligned}
\tag{54}
$$

The undercooling of the melt is the sum of the solute undercooling [Eq. (54)] and of the capillary undercooling [Eq. (13)], or as stated in Eq. (55).

$$\Delta T_S = \Delta T - \Delta T_{cap} \tag{55}$$

During the growth, the system is cooled at a rate P and the latent heat is released proportionally to the increase of the solid fraction, so the variation of liquid undercooling is given by Eq. (56).

$$\frac{d\Delta T}{dt} = P - \frac{\Delta H_m}{C_p}\frac{df_s}{dt} \tag{56}$$

Equations (53–56) form a system into which the number of particles, their size, and the undercooling enter as unknown variables. This system can be solved numerically if an initial value is given for the radius r_0.

The third step starts when the temperature of the melt increases enough to stop the grain nucleation. No more grains are formed, but the other grains continue growing and it has been shown that it is during this step that they are destabilized and show dendrite arms.

This model is able to reproduce the melt undercooling, the undercooling breakdown, and the recalescence, and, most importantly, gives the tendencies concerning the final number of grains. Some interesting results are shown in Fig. 3.39. The contact angle of the seed on the foreign particle has a huge influence on the number of grains. It is also shown that the cooling rate is likely to help to control the number of grains.

Finally, the model is able to explain the experimental fact that the grain size decreases with the number of refining particles, but only to a certain extent. If too many particles are present, the number of growing grains increases quickly at the beginning and the latent heat released prevents the nucleation of other grains. It is then possible to determine the number of foreign particles leading to the smallest grains. However, the model remains only qualitative.

Greer has proposed an improvement of the previous model, taking into account the statistical distribution of particle size and a free growth of the dendrites

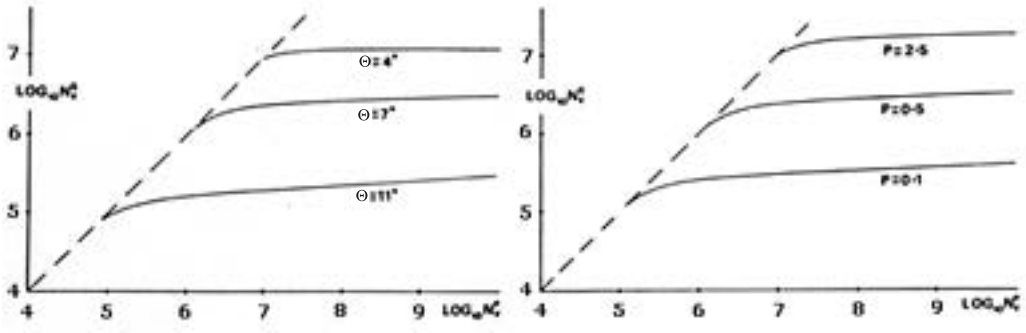

Fig. 3.39 Equiaxed grain density versus foreign particle density. Parameter: contact angle for $P = 0.5$ K s^{-1} (left), and cooling rate for $\theta = 7°$ (right) (Al–Ti, $r_0 = 1$ μm) (Maxwell and Hellawell 1975).

(Greer et al. 2000). This analysis has been performed in the case of Al alloy casting with Al-Ti5-1B as refiner.

Suppose that Al seeds nucleate on the large [0001] faces of TiB_2 particles: if the wetting angle is low enough, this is likely to happen at low undercoolings. The Al seed grows laterally and when the face is covered, it keeps on growing, but with an increase in the curvature of the solid–liquid interface (Fig. 3.40). The radius of curvature of the nucleus cannot be lower than the critical radius for nucleation, r^*, which depends on the undercooling [Eq. (12)]. Therefore free growth occurs only when the critical radius becomes lower than the particle radius. It follows that, for a particle population ranging from 0.1 to 10 μm, this kind of free growth occurs for undercoolings from 6–0.06 K, which indeed corresponds to the undercoolings observed in the processing of refined Al alloys.

It follows also that during the liquid cooling seeds appear first on large particles then on smaller and smaller particles when the undercooling increases.

Greer's model then adopts Maxwell–Hellawell's treatment, where the growth of existing seeds causes a decrease in the undercooling and of the subsequent recalescence. This means that all the particles under a certain diameter do not lead to

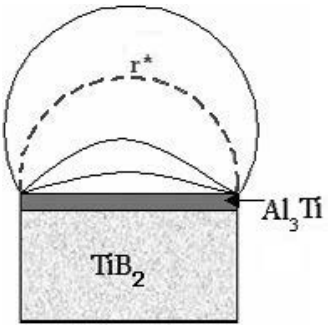

Fig. 3.40 Growth of Al seed on the Al-Ti5-1B refiner particle.

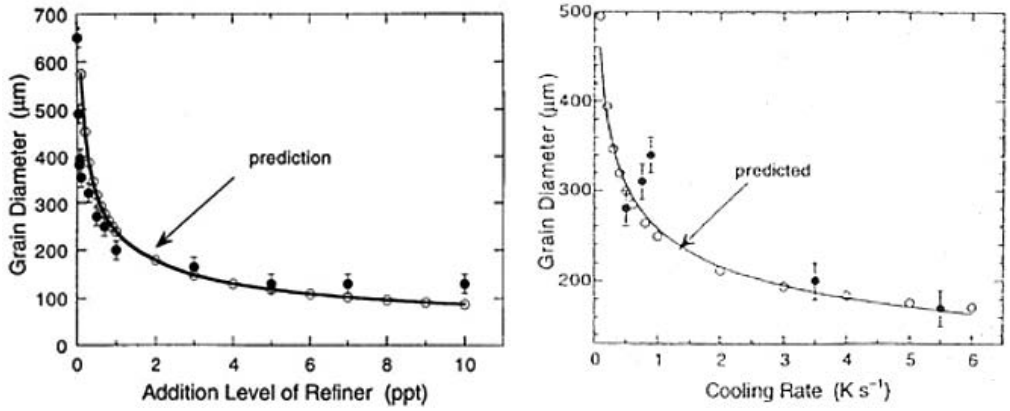

Fig. 3.41 Variation of grain size with refiner quantity and with cooling rate, as predicted by Greer's model and compared to experimental values (Greer et al. 2000).

seed nucleation because the undercooling does not decrease sufficiently. In practice only 5% of the particles are useful for seeding, but, as they are the biggest ones, these represent a significant part of the refiner mass.

The prediction of the grain size versus quantity of refiner and cooling rate agrees quantitatively with the experimental observations (Fig. 3.41) and shows that above a quantity of about 1 ppt (part per thousand) (by weight) of refiner, or a cooling rate of 1 K s^{-1}, a further increase is not useful for decreasing the grain size. It is worth noting that the model does not use any adjustable parameter.

It should be noted that the model is based on the hypothesis that the nucleation on the particle is easy (i.e., the contact angle is low) and therefore cannot be applied if the nucleation barrier is too large. It has been remarked that certain solutes, such as Zr, have a strong effect on the nucleation properties and thus act as killers of the refining effect.

3.3.2.2 **Columnar to Equiaxed Transition**

As shown in the introduction to Section 3.3.2, columnar and equiaxed transitions are competing at some moment of the ingot solidification. It therefore is important to know when the transition between the two structures will occur and what the parameters influencing this transition are.

The classical model has been proposed by Hunt (1984). A columnar dendritic interface is growing; its growth rate is imposed by the heat extraction through the mold (constrained growth). The dendrite tip undercooling is self-adjusted to the given velocity (see Section 3.2.2.2). A region of undercooled liquid is thus created ahead the columnar front, whose extent and undercooling depend on the solidification rate and temperature gradient. It is supposed that solid seeds are nucleating (in the presence of refining particles) in this undercooled region and grow as equiaxed dendrites. The structure will remain columnar if the volume of

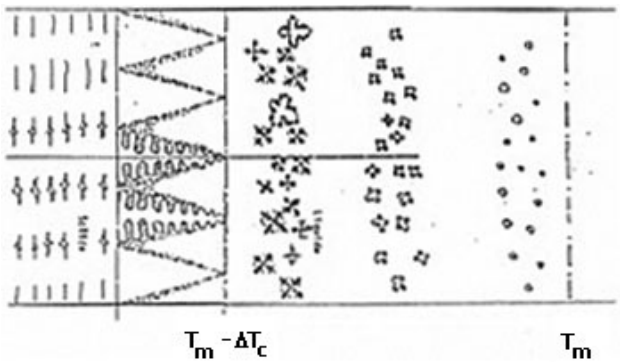

Fig. 3.42 Schematic plot of the competition between columnar and equiaxed growths. The columnar front is undercooled by ΔT_c and seeds nucleate in the liquid below the melting temperature T_m and then grow, as the columnar front is approaching.

equiaxed grains is negligible compared with the advancement of the columnar front. Conversely, if the equiaxed grains grow fast enough to occupy the major part of the volume before being passed by the columnar font, the resulting structure will be equiaxed.

The nucleation rate is expressed, from Eq. (53), taking into account the remaining number of free nucleating particles, as Eq. (57).

$$\frac{dN}{dt} = (N_0 - N) I_0 e^{-\Delta G_n / k_B T} \tag{57}$$

An undercooling is necessary for nucleation [ΔG_n varies as $1/\Delta T_N{}^2$; compare Eq. (3.51)]. At the columnar dendrite tip, the undercooling is maximal and equal to ΔT_c and it follows that there are two situations:

- if $\Delta T_N > \Delta T_c$, the equiaxed dendrites cannot nucleate and no equiaxed grain will appear
- if $\Delta T_c > \Delta T_N$, seeds will nucleate at the forefront of the columnar tips, and as Eq. (30b) states, the growth rate of these equiaxed dendrites is proportional to the square of the local undercooling [Eq. (58)].

$$\frac{dr}{dt} = \frac{D_l}{4 C_0 m_l (k-1) \Gamma} \Delta T^2 \tag{58}$$

This local undercooling varies between ΔT_N and ΔT_c at a rate depending on the velocity of the columnar front and on the thermal gradient in the liquid [Eq. (59)].

$$\frac{d\Delta T}{dt} = v_i \nabla T \tag{59}$$

When the equiaxed dendrite comes into contact with the columnar front, its radius is given by Eq. (60) and the volume of equiaxed grains formed per unit of time by Eq. (61).

$$r = \frac{D_l}{4C_0 m_l (k-1)\Gamma} \int_0^t \Delta T^2 \, dt = \frac{D_l}{4C_0 m_l (k-1)\Gamma} \int_{\Delta T_N}^{\Delta T_C} \frac{\Delta T^2}{v_i \nabla T} d\Delta T \tag{60}$$

$$V_{eq} = N_0 \frac{4}{3} \pi r^3 \tag{61}$$

Hunt considered that the structure will be equiaxed if this volume is more than 66% of the total volume solidified per unit time (at the velocity v_i) and columnar if it is less than 0.66%. It finally follows that the structure is columnar if Eq. (62a) is satisfied, and equiaxed if Eq. (62b) is true.

$$\nabla T > 0.617(100N_0)^{1/3}(1 - \Delta T_N^3/\Delta T_c^3)\Delta T_c \tag{62a}$$

$$\nabla T < 0.617{N_0}^{1/3}(1 - \Delta T_N^3/\Delta T_C^3)\Delta T_c \tag{62b}$$

Between these two values, the structure is a mixture of columnar and equiaxed grains. ΔT_c is linked to the growth rate v_i through Eqs. (27) and (28).

The effect of the leading parameters is plotted in Fig. 3.43. For a given thermal gradient, the equiaxed growth is possible only at high velocity, because at low velocity the undercooling is too small to allow for seed nucleation. Increasing the thermal gradients helps the columnar growth, because the thickness of the undercooled layer depends on the thermal gradient. This is the reason why equiaxed grains are observed frequently at the end of the solidification, when the liquid becomes almost isothermal.

The limiting velocity below which no equiaxed grain can nucleate decreases when the solute concentration increases and when the nucleation undercooling decreases (Fig. 3.44).

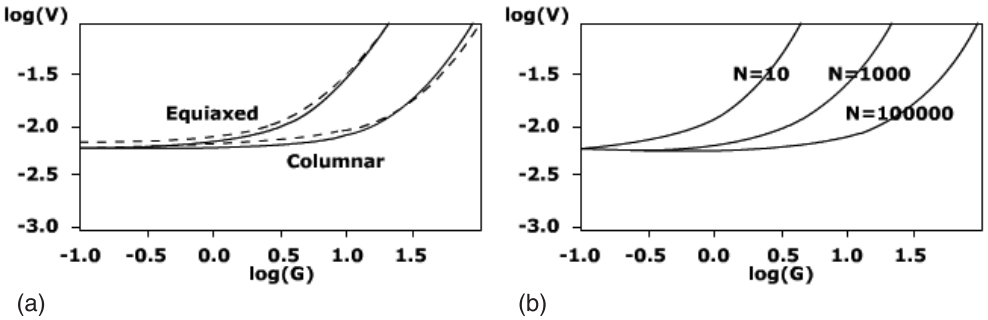

Fig. 3.43 (a) Equiaxed and columnar domains in a $v_i/\nabla T$ diagram, and (b) effect of the number of refining particles on the equiaxed side of the transition. Al–3%Cu (Hunt 1984).

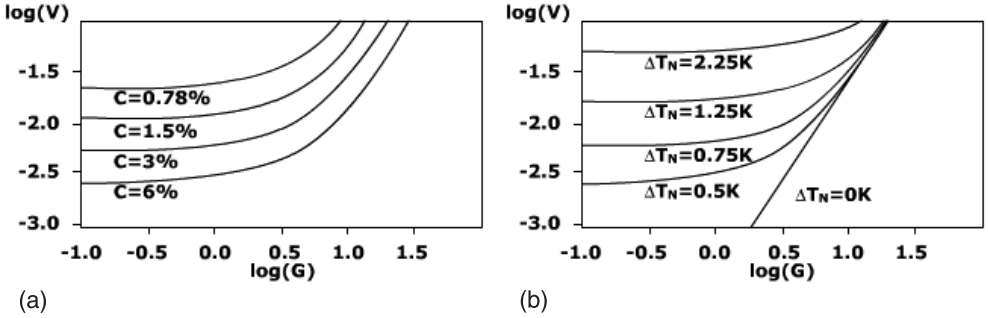

Fig. 3.44 Equiaxed and columnar domains in diagrams showing growth rate versus thermal gradient. (a) Effect of the alloy composition and (b) of the nucleation undercooling on the equiaxed side of the transition. Al–3%Cu (Hunt, 1984) .

The model neglects convective effects, which are known to be strong, because in reality there is transport of the smallest equiaxed grains by the convective flow, into regions where they may melt back. Larger grains tend toward sedimentation. In any case, the model is useful as it helps an understanding of the leading parameters acting on the columnar equiaxed transition. Experiments performed under microgravity conditions in order to avoid any convective perturbations have made it possible to discuss the validity of the model, which is limited by its sensitivity to the initial parameters (undercooling and number of seeds) (Dupouy and Camel 2001).

3.3.3
Macro- and Mesosegregation

In this section, perturbations of the columnar dendritic field are discussed. The region between the tip and the bottom of the dendrite, where solid and liquid exist simultaneously, is often called the ''mushy zone''. Neglecting the undercooling of the tip, its thickness can be calculated through Eq. (63) (see Fig. 3.16).

$$a = \frac{\Delta T_0}{\nabla T} \tag{63}$$

This mushy zone in certain solidification processes may reach several decimeters. The thermal and chemical characteristics of the mushy zone are directly related to the dendrite, as studied in Section 3.2.2. However it also has a strong interaction with the flow field, acting as a porous medium (Darcy flow), with the particularity that the permeability depends on the solidification conditions, which in turn are influenced by the flow field (see Fig. 3.13). By changing the thermal and solutal fields around the dendrite, and inside the dendritic field, convective flows have a strong influence on the solidification conditions. The coupling of

the interdendritic flow with hydrodynamics in the bulk liquid leads to defects in the material and chemical segregations on the ingot scale. The chemical segregation is called ''positive'' where the local chemical composition is higher than the mean ingot concentration, and ''negative'' where it is lower.

Independently of forced convection that may be imposed on the system (through mechanical, electromagnetic, or other processes), natural convection always exists because of the thermal field perturbation by the solidification front, but also, and even more so, because of the chemical gradients that induce variations in the liquid density. Both thermal and solutal fields are acting on the liquid density through their expansion coefficients [Eq. (64)].

$$\rho_l = \rho_l^0(1 + \beta_T \Delta T + \beta_C c_l). \tag{64}$$

Since the chemical and thermal fields are related by the thermodynamic equilibrium hypothesis along the dendrite side [Eq. (3)], Eq. (65) follows.

$$\rho_l = \rho_l^0\left(1 + \left(\beta_T + \frac{\beta_C}{m_l}\right)\Delta T\right) \tag{65}$$

The thermal expansion coefficient is of the order 10^{-4} K^{-1} and the chemical term in Eq. (64) is of the order of 10^{-2}–10^{-3} K^{-1}. Therefore the thermal convection within the mush can generally be neglected. The resulting Archimedes force is calculated through Eq. (66).

$$F_p = \beta_C \Delta T g / m_L \tag{66}$$

It follows that the convective effects will depend on the orientation of the solute gradients relative to gravity.

From a solute balance at the local scale, Flemings and Nereo (1967) derived the equation of solute distribution [Eq. (67)], taking into account the local convective flow.

$$\frac{\partial f_l}{\partial c_l} = -\frac{(1-\delta_\rho)}{(1-k)}\left(1 + \frac{v_l.\nabla T}{v_i.\nabla T}\right)\frac{f_l}{c_l}, \tag{67}$$

Here δ_p is the solidification shrinkage, and v_l the liquid velocity, which is given by Darcy's law, with a permeability factor depending on the liquid fraction according to Eq. (68).

$$v_l = \frac{-K}{\mu f_l}(\nabla p - \rho_l g) \quad K = a f_l^2 \tag{68}$$

If there is no convection and no shrinkage, Eq. (67) is the differential form of the classical Scheil's law, Eq. (10). If convection is insignificant or parallel to the thermal gradient, integration of Eq. (67) gives a modified Scheil's law, Eq. (69).

$$c_l = c_0(1 - f_s)^{(k-1)/(1-\delta_\rho)} \tag{69}$$

Transition toward the convective regime occurs when the fluid velocity becomes of the same order as the growth rate.

In order to show the effect of the orientation of the thermal gradient (or equivalently, of the growth direction) versus gravity, examples of solidification of Al–Cu alloys grown for various configurations are shown below. Considering the complexity of the interactions and coupled mechanisms involved, only qualitative arguments will be given.

Six configurations exist, depending on the direction of solidification (horizontal, vertical upward, and vertical downward) and on the alloy concentration: hypo-eutectic (the rejected Al is lighter than the Cu solvent) or hyper-eutectic (the rejected Cu is heavier than the Al solvent). These can be grouped into three different convective situations: horizontal, vertical with solute stabilization of the liquid (Al-rich downward or Cu-rich upward), and vertical with solute destabilization of the liquid (Al-rich upward or Cu-rich downward).

The hypo-eutectic horizontal case is shown in Fig. 3.45. Dendrites are located at the bottom of the ingot cross-section because the flow, driven by the rising of the Al-enriched liquid, increases the chemical composition at the top, where the eutectic grows. Conversely, in the case of a hyper-eutectic alloy, the eutectic is located at the bottom and the dendrites at the top.

In the vertically destabilizing case (Fig. 3.46) the liquid is unstable and driven away from the interface, which creates convective chimneys in the dendritic field. The solute is carried through the mush to those particular places, where the concentration increases and a purely eutectic structure may eventually form. This causes freckles in the solid; such freckles are extremely detrimental to the mechanical properties of the alloy.

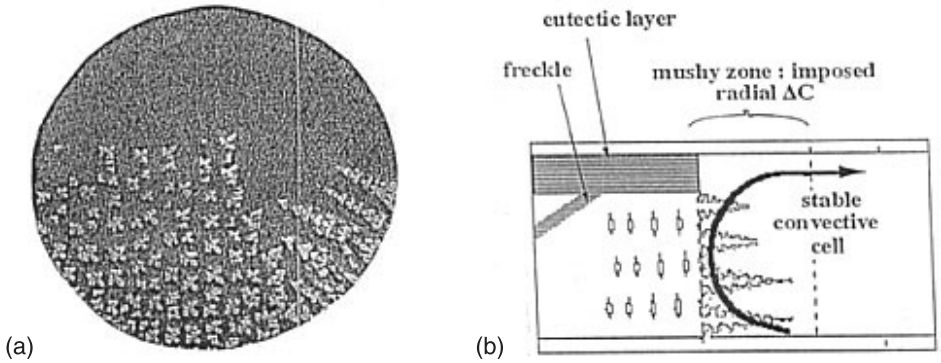

Fig. 3.45 Effect of convection on the structure of a horizontally solidified Al-rich Al–Cu alloy; (a) metallographic picture in cross-section; (b) sketch of the flow and its effect on the microstructure (Dupouy and Camel 2000).

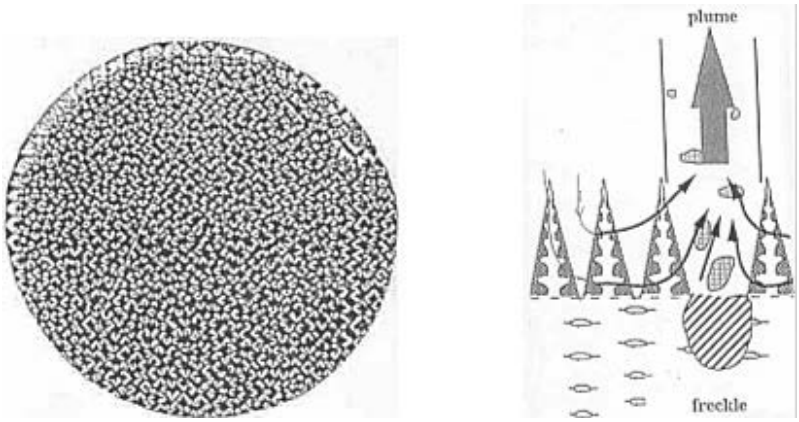

Fig. 3.46 Effect of convection on the structure of an Al–Cu alloy grown under vertically destabilized configuration: downward solidification of a hyper-eutectic alloy. One freckle appears here as a region with smaller dendrites (Dupouy and Camel 2000).

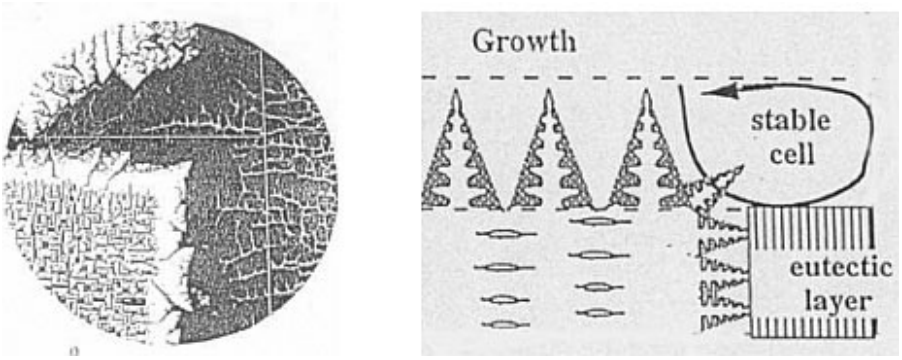

Fig. 3.47 Effect of convection on the structure of an Al–Cu alloy grown under vertically stabilizing configuration: upward solidification of a Cu-rich alloy (Dupouy and Camel, 2000).

The vertically stabilizing case is shown in Fig. 3.47. No interdendritic flow would be expected if the isoconcentrations were strictly planar and horizontal. However, defects inside the dendritic field induce radial solute gradients which force convective loops in the mushy zone, and cause radial segregation, possibly leading to the formation of purely eutectic regions as in the example shown. However, contrarily to the previous case, the average concentration in a cross-section remains equal to the nominal concentration (absence of longitudinal segregation).

3.4 Outlook

The objectives of this chapter have been to introduce the reader to the fundamental aspects of solidification in a simplified way, to show the basic physical phenomena involved in structure formation of alloys, and to explain the generation of defects during solidification.

The most important parameter determining all the solidification-related phenomena is the undercooling of the solid–liquid interface, which depends essentially on the local chemical composition and curvature. The kinetic undercooling is negligible in the case of metallic alloys which present a rough interface, but may reach several Kelvins for materials exhibiting faceted growth, such as intermetallics or semiconductors.

Therefore the structuring of the alloy is the result of the competition between:

- diffusion in the liquid, which governs the chemical field close to the interface: solutal undercooling decreases as microstructure size decreases
- capillary forces: capillary undercooling decreases as microstructure size increases.

This competition is active continuously in all structuring processes: interface destabilization and formation of dendrites, cells, eutectics, and grains.

Simultaneously, the solid–liquid interface interacts with the surroundings. The essential external parameter acting on solidification is the thermal field applied to the alloy through the heat fluxes extracted, or generated, in the growth facility. This heat extraction is responsible for the spatial temperature distribution, acting on most of the structuring processes through the thermal gradient, and for the temperature variation with time, which fixes the growth rate.

Defects are related to foreign elements, which lead to chemical segregation, nucleation of particles or bubbles, or act as nucleating agents. A second effect concerns the interaction of convection with the solidification process through perturbation of the thermal and chemical fields. It should be kept in mind that the convective patterns are often coupled with the solidification process. This is a consequence of the solute rejection in the liquid, which makes the problem extremely difficult to tackle.

Owing to such complexity, the present development in solidification research tends essentially toward numerical simulation. This is the only way to get explanations or predictive conclusions in the industrial processes, which are geometrically complex and time-dependent. Currently, software is being developed in order to fully solve the problem in real configuration, computing the temperatures, velocities, solute field, and structures (dendrite or eutectic sizes, etc.). The models generally take into account the mechanical evolution of the material after solidification and the associated defect generation.

Numerical simulation is also at the forefront of more fundamental research, especially by the use of phase field simulation techniques, which give new insight into the structuring phenomena and their interaction with the surroundings.

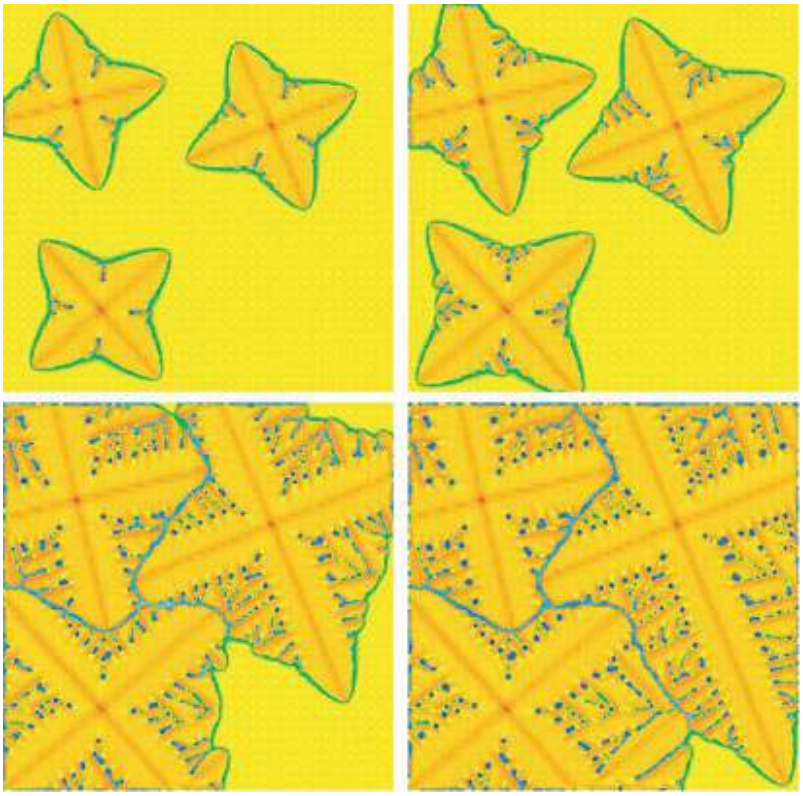

Fig. 3.48 Phase field simulation of equiaxed growth. Three equivalent seeds are introduced into an undercooled melt. At the end of the growth, the equiaxed grains are closely connected to each other. The blue color in the last picture represents liquid which is unsolidified due to solute rejection and trapping in the dendrite arms or between the grains.

This numerical technique is particularly well adapted to take into account the complex shape of the solid–liquid interface. An example of simulation of equiaxed growth is given in Fig. 3.48. A comprehensive review of this contribution can be found in Boettinger et al. (2002) and partially in the introduction to phase field methods given in Chapter 10.

Acknowledgments

The author expresses his gratitude to Dr. Denis Camel and Dr. Carmen Stelian for their help in carefully reading and correcting this chapter. The help of the Editor, Prof. Pfeiler, has also been very much appreciated.

Nomenclature

a	lattice parameter, structural unit size
$\boldsymbol{b}$	Burgers vector
c	chemical composition
f	fraction (of solid or liquid)
$\boldsymbol{g}$	gravity vector
h	vacancy or hole
k	segregation coefficient
k_B	Bolzmann constant
m	liquidus or solidus slopes
p	pressure
r	radius (of nuclei, of curvature, of dendrite tip ...)
$\boldsymbol{u}$	fluid velocity
v	solid–liquid interface velocity
x	mole fraction
x, y, z	axes

C_p	heat capacity
D	diffusion coefficient
E	Young's modulus
Gr	Grashof number
G	Gibbs free energy
H	enthalpy
I	nucleation rate (s^{-1})
$J, \boldsymbol{j}$	flux and flux density
K	kinetic coefficient or permeability coefficient in Darcy's law
N	a number (of nuclei, particles etc.)
Pe	Peclet number
R	ideal gas constant
Re	Reynolds number
S	entropy
T	temperature
V	volume (V_a, atomic volume)

α	Jackson's reduced transformation entropy
α	thermal dilatation coefficient
β	solutal dilatation coefficient
γ	surface energy (solid–liquid, liquid–gas etc.)
δ	boundary layer thickness
δ_ρ	relative density jump aty the interface $(\rho_s - \rho_l)/\rho_l$
ε	fluctuation, strain, perturbation
κ	curvature $(1/r)$
λ	characteristic solidification structure periodicity or length
μ	viscosity
σ	stress

Γ	Gibbs parameter ($\gamma/\Delta S$, Km)
Λ	thermal conductivity
ΔG, ΔH, ΔS	formation/migration/etc. energy values (differences)
ΔT	undercooling
Δc	supersaturation
θ	contact angle
Ω	reduced supersaturation
∇	gradient

Subscripts or superscripts

cap	capillary
s	solid
l	liquid
i	at the solid–liquid interface
m	melting
0	reference
ch	chemical
S	surface
T	thermal

References

Aaron H. B., Fainstein D., Kotler G. R. (1970), *J. Appl. Phys.* **41**, 4404–4410.

Access-Aachen, from the CD-Rom *Materials in Focus*, Access-RWTH, Intzestr., 5, Aachen, Germany.

Aziz M. J. (1982), *J. Appl. Physics* **53**, 1158–1168.

Bennema P. (1993), ''Growth and morphology of crystals'' in *Handbook of Crystal Growth Vol. 1a*, D. T. J. Hurle Ed., North Holland, pp. 477–581.

Boettinger W. J., Warren J. A., Beckermann C., Karma A. (2002), *Annu. Rev. Mater. Res.* **32**, 163–194.

Boiton P., Giacometti N., Duffar T., Santailler J. L., Dusserre P., Nabot J. P. (1999), *J. Crystal Growth* **206**, 159–165.

Burton W. K., Cabrera N., Frank F. C. (1951), *Phil. Trans. Roy. Soc.* **A243**, 299–358.

Burton J. A., Prim R. C., Schlichter W. P. (1953), *J. Chem. Phys.* **21**, 1987–1991.

Cahn J. W. (1960), *Acta Met.* **8**, 554–562.

Chernov A. A., De Yoreo J. J., Rashkovich L. N., Vekilov P. G. (2004), *MRS Bull.* **29**, 927–934.

Coriell S. R., McFadden G. B. (1993), ''Morphological stability'' in *Handbook of Crystal Growth Vol. 1b*, D. T. J. Hurle Ed., North Holland, pp. 785–857.

Dash W. C. (1959), *J. Appl. Phys.* **30**, 459–474.

Duffar T., Dusserre P., Giacometti N., Boiton P., Nabot J. P., Eustathopoulos N. (1999), *J. Crystal Growth* **198–199**, 374–378.

Dupouy M. D. (1986), PhD Thesis, INP-Grenoble (March 27).

Dupouy M. D., Camel D. (2000), *Recent Developments in Crystal Growth Research*, Ed., **2**, 179–210, Transworld Research Network.

Dupouy M. D., Camel D. (2001), *J. Phys. IV* **11**, 119–126.

Dupouy M. D., Camel D., Favier J. J. (1992), *Acta Metall. Mater.* **40**, 1791–1801.

Dupouy M. D., Camel D., Mazille J. E. (2003), *Proc. Int. Conf. Modelling of Casting, Welding and Adv. Solidification Process X*, Destin, Florida, USA, May 25–30, D. Stefanescu et al. Ed.,TMS, pp. 685–692.

Esaka H. (1986), ''Dendrite growth and spacing in succinonitrile–acetone alloys,'' PhD Thesis, École Polytechnique Fédérale de Lausanne, Switzerland.

Feurer U., Wunderlin R. (1977), *Fachb. Deuts. Ges. Metallk.*, Oberursel, FRG, cited in Kurz and Fischer (1998).
Flemings M. C. (1974), *Solidification Processing*, Mc Graw-Hill, New York.
Flemings M. C., Nereo G. E. (1967), *Trans. Met. Soc. AIME* **239**, 1449, cited in Flemings (1974).
Gandin C. A., Rappaz M. (1994), *Acta Metall. Mater.* **42**, 2233–2246.
Garandet J. P., Favier J. J., Camel D. (1994), ''Segregation phenomena in crystal growth from the melt'' in *Handbook of Crystal Growth Vol. 2b*, D. T. J. Hurle Ed., North Holland, pp. 659–707.
Gerardin S., Combeau H., Lesoult G. (2001), *J. de Physique IV* **Pr6**-143.
Gondet S., Louchet F., Théodore F., Van den Bogaert N., Santailler J. L., Duffar T. (2003), *J. Crystal Growth* **252**, 92–101.
Greer A. L., Bunn A. M., Tronche A., Evans P. V., Bristow D. J., *Acta Mater.* (2000) **48**, 2823–2835.
Hoyt J. J., Asta M., Haxhimali T., Karma A., Napolitano R. E., Trivedi R., Laird B. B., Morris J. R. (2004), *MRS Bull.* **29**, 935–939.
Huang S. C., Glicksman M. E. (1981), *Acta Met.***29**, 701–715 and 717–734.
Hunt J. D. (1984), *Mater. Sci. Eng.* **65**, 76–83.
Hurle D. T. J. (1995), *J. Crystal Growth* **147**, 239–250.
Hurle D. T. J., Rudolph P. (2004), *J. Crystal Growth* **264**, 550–564.
Ivantsov G. P. (1947), *Dokl. Akad. Nauk USSR* **58**, 567–569.
Jackson K. A. (1958) in *Liquid Metals and Solidification*, American Society of Metals.
Jackson K. A., Hunt J. D. (1966), *Trans. Met. Soc. AIME* **236**, 1129–1142.
Jackson K. A., Hunt J. D., Uhlmann D. R., Seward T. P. (1966), *Trans. Met. Soc. AIME* **236**, 149–158.
Johnson W. L. (1999), *Mater. Res. Soc. Symp. Proc.* **554**, 311–339.
Jones H. (1984), *J. Mater. Sci.* **19**, 1043–1076.
Kattamis T. Z., Flemings M. C. (1965), *Trans. Met. Soc. AIME* **233**, 992–999.
Kurz W., Fischer D. J. (1998), *Fundamentals of Solidification*, TransTech Publications.
Kurz W., Trivedi R. (1990), *Acta Metall. Mater.* **38**, 1–17.
Lagowski J., Gatos H. C., Parsey J. M., Wada K., Kaminska M., Walukiewicz W. (1982), *Appl. Phys. Lett.* **40**, 342–344.
Langer J. S., Müller-Krumbhaar H. (1977), *J. Crystal Growth* **42**, 11–14.
Maxwell I., Helawell A. (1975), *Acta Met.* **23**, 229–237.
Mullins W. W., Sekerka R. F. (1964), *J. Appl. Phys.* **35**, 444–451.
Rappaz M., Gandin C. A. (1993), *Acta Metall. Mater.* **41**, 345–360.
Scheil E. (1942), *Zeit. Metall.* **34**, 70–72.
Sekerka R. F. (1965), *J. Appl. Phys.* **36**, 264–268.
Tiller W. A., Jackson K. A., Rutter J. W., Chalmers B. (1953), *Acta Met.* **1**, 428–437.
Trivedi R., Somboonsuk K. (1984), *Mater. Sci. Eng.* **65**, 65–74.
Völkl J. (1994), ''Stress in the cooling crystal'' in *Handbook of Crystal Growth Vol. 2b*, D. T. J. Hurle Ed., North Holland, pp. 821–874.
Wenzl H., Dahlen A., Fattah A., Petersen S., Mika K., Henkel D. (1991) **109**, 191–204.